IPEM
Institute of Physics and
Engineering in Medicine

PAPER • OPEN ACCESS

Experimental demonstration of accurate Bragg peak localization with ionoacoustic tandem phase detection (iTPD)

View the article online for updates and enhancements.

Physics in Medicine & Biology

IPEM Institute of Physics and Engineering in Medicine

PAPER

Experimental demonstration of accurate Bragg peak localization with ionoacoustic tandem phase detection (iTPD)

H P Wieser[1,6] , Y Huang[2,3,6] , J Schauer[4,6], J Lascaud[1] , M Würl[1] , S Lehrack[1], D Radonic[1], M Vidal[5], J Hérault[5], A Chmyrov[2,3], V Ntziachristos[2,3], W Assmann[1], K Parodi[1] and G Dollinger[4]

1   Department for Medical Physics, Faculty of Physics, Ludwig-Maximilians-Universität München, D-85748 Garching b. München, Germany
2   Chair of Biological Imaging (CBI) and Center for Translational Cancer Research (TranslaTUM) Technical University Munich, D-81675 Munich, Germany
3   Institute of Biological and Medical Imaging (IBMI), Helmholtz Zentrum München, D-85764 Neuherberg, Germany
4   Institute for Applied Physics and Metrology, Department of Aerospace Engineering, Universität der Bundeswehr München, D-85577 Neubiberg, Germany
5   Centre Antoine Lacassagne—Fédération Claude Lalanne, 227 avenue de Lanterne, F-06200 Nice, France
6   Equal contribution.

E-mail: H.Wieser@physik.uni-muenchen.de and Katia.Parodi@physik.uni-muenchen.de

Abstract

Accurate knowledge of the exact stopping location of ions inside the patient would allow full exploitation of their ballistic properties for patient treatment. The localized energy deposition of a pulsed particle beam induces a rapid temperature increase of the irradiated volume and leads to the emission of ionoacoustic (IA) waves. Detecting the time-of-flight (*ToF*) of the IA wave allows inferring information on the Bragg peak location and can henceforth be used for *in-vivo* range verification. A challenge for IA is the poor signal-to-noise ratio at clinically relevant doses and viable machines. We present a frequency-based measurement technique, labeled as ionoacoustic tandem phase detection (iTPD) utilizing lock-in amplifiers. The phase shift of the IA signal to a reference signal is measured to derive the *ToF*. Experimental IA measurements with a 3.5 MHz lead zirconate titanate (PZT) transducer and lock-in amplifiers were performed in water using 22 MeV proton bursts. A digital iTPD was performed *in-silico* at clinical dose levels on experimental data obtained from a clinical facility and secondly, on simulations emulating a heterogeneous geometry. For the experimental setup using 22 MeV protons, a localization accuracy and precision obtained through iTPD deviates from a time-based reference analysis by less than 15 μm. Several methodological aspects were investigated experimentally in systematic manner. Lastly, iTPD was evaluated *in-silico* for clinical beam energies indicating that iTPD is in reach of sub-mm accuracy for fractionated doses < 5 Gy. iTPD can be used to accurately measure the *ToF* of IA signals online via its phase shift in frequency domain. Further developments are required to reach <1Gy detection capabilities for clinical application. iTPD may become a useful tool especially when a decisive frequency is present in the acoustic signal.

1. Introduction

The number of cancer patients being treated worldwide with accelerated ions is rising because of their wider spread instrumentation and the interest to exploit their advantageous dosimetric properties compared to conventional irradiation with high-energetic photons. The physical advantages are mainly due to the characteristic inverse depth dose profile, the so-called Bragg curve, and its steep dose-fall off (finite range). These features make it possible to confine high homogeneous radiation doses to cancerous tissue while keeping the integral dose to organs at risk and normal tissue low (Newhauser and Zhang 2015, Baumann *et al* 2016). Although the acceleration energy of ions and therewith the ion range can be controlled precisely from a technical standpoint, their predicted Bragg peak location within the patient cannot.

The imprecise knowledge of Bragg peak locations during treatment relates among others to inaccuracies in the derivation of ion stopping powers in tissue (relative to water) from x-ray computed tomography (CT) and to anatomical changes causing ions to penetrate different tissue densities than planned. In practice, dose calculation and optimization are based on a CT scan acquired before patient irradiation. Anatomical changes between the planning CT and actual irradiation (inter-fractional) as well as movements within irradiation (intra-fractional) yield varying ion ranges and might result subsequently in sub-optimal patient treatments (Lomax 2008a, 2008b, Paganetti 2012).

Ion range uncertainties are addressed by pre-treatment mitigation approaches such as advanced imaging (ion radio-tomography (Johnson 2018), dual-energy CT (Wohlfahrt *et al* 2018)), dose calculation/prediction algorithms (Kozłowska *et al* 2019), safety margins (Van Herk 2004) and robust planning (Unkelbach *et al* 2018). Additionally, there are also approaches being investigated to verify the ion range *in-vivo* during irradiation. Such *in-vivo* verification methods potentially provide immediate feedback on the dose deposition of the ongoing treatment. The two most prominent approaches can be grouped into prompt gamma monitoring resolving spatial information and/or time, energy (Verburg and Seco 2014, Richter *et al* 2016, Krimmer *et al* 2018, Hueso-González *et al* 2018, Parodi and Polf 2018, Dal Bello *et al* 2020, Parodi 2020, Pausch *et al* 2020) and positron emission tomography resolving spatial information (Vynckier *et al* 1993, Parodi *et al* 2007, Bisogni *et al* 2016, Buitenhuis *et al* 2017, Ferrero *et al* 2018). Both methods are based on the detection of secondary emissions induced by nuclear interactions between primaries and the target nuclei. These secondary signatures enable the indirect derivation of the Bragg peak location in room coordinates by comparing measurement against simulations. Thus the Bragg peak or proton range can be mapped onto the CT scan to detect ion under- or over-shoots from the initially planned stopping location. One advancement is prompt gamma spectroscopy which allows to infer the elemental composition of the irradiated tissue.

Another *in-vivo* range verification method, based on the ionoacoustic (IA) effect, re-emerged in the past years. The localized energy deposition from an ion pencil beam with a short rise time yields to a thermoelastic expansion provoking an IA wave (Assmann *et al* 2015, Jones *et al* 2016a, Hickling *et al* 2018). The IA wave encodes information of the underlying dose distribution and can be measured with acoustic sensors on the patient's surface (Hayakawa *et al* 1995). The IA signal shape allows to infer dose deposition characteristics, for instance, through dose reconstruction methods Yu *et al* (2019) while the acoustic time-of-flight (*ToF*) only allows Bragg peak localization. An overview of techniques to approximate the *ToF* can be found in Jones *et al* (2016b). Measuring the *ToF* ultimately at multiple locations on the patient skin allows to reconstruct the maximum Bragg peak location in 3D.

The work of Patch *et al* (2016, 2019, 2021) investigated thermoacoustic range verification in combination with co-registered ultrasound (US) images. It was concluded that an online thermoacoustic verified ion range marked on US is feasible if the treatment target is visible in the US image or can be registered to the CT. Moreover, Kellnberger *et al* (2016) demonstrated IA tomography imaging of the Bragg peak in co-registered US and optoacoustic images for irradiation of a mouse leg.

It is important to stress that, if adequately pulsed, the frequency of IA signals is inversely proportional to the beam energy. Lower beam energies (22 MeV) produce IA frequencies of up to several MHz while higher clinical beam energies generate IA frequencies typically below 200 kHz.

For clinical proton energies from 75 to 220 MeV, the IA pressure amplitude is below 100 mPa considering a pulse width of 4 μs, a charge of 2 pC per pulse and a sensor a few cm away from the Bragg peak (Lehrack *et al* 2017, van Dongen *et al* 2019). Both, the low amplitude and low frequency of the IA signal only partially match the sensitivity of current detector technologies resulting in a poor signal-to-noise ratio (SNR) at clinically relevant dose levels. For instance, it was necessary in a previous study (Lehrack *et al* 2017) to average 1000 measurements from a triggered data acquisition (total Bragg peak dose of 10 Gy) to achieve a range precision below 1 mm for a 220 MeV clinical proton beam stopping in water. Nonetheless, the number of repetitive measurements N is restrained by the prescribed dose and becomes, for large number of averages N due the direct relation of SNR on the square root of N, ineffective.

To increase the SNR, Otero *et al* (2020) presented a method to optimize the piezoelectric sensor geometry (thickness and diameter) to increase the sensitivity for clinical IA signals. Moreover, Riva *et al* (2018) and Vallicelli *et al* (2021) developed a dedicated analog–digital front-end electronic, while Sohn *et al* (2020) brought forward a wavelet filtering technique to enhance the IA signal by means of post-processing. Recently, Freijo *et al* (2021) presented a dictionary based acoustic proton range verification approach utilizing prior information from simulations.

Although several IA related simulation studies (Jones *et al* 2018, Patch *et al* 2018, Takayanagi *et al* 2019, van Dongen *et al* 2019, Yu *et al* 2019, Freijo *et al* 2021), have been carried out recently, only little progress has been made on the signal detection side.

Therefore, we present in this manuscript a frequency based measurement technique using lock-in amplifiers aiming to overcome the poor SNR in time domain at clinical dose levels. Mascarenhas *et al* (1984) proposed an

optoacoustic (OA) radiation dosimeter utilizing a lock-in amplifier. The idea was to detect x-ray induced OA signals for absolute radiation dosimetry. We extend this concept one step further to IA and focus on measuring the *ToF* which relates to the distance between Bragg peak maximum and the acoustic sensor.

The presented method is stimulated by the patent depicted in Dollinger *et al* (2016) and proposed to measure the *ToF* of the IA wave from its phase shift in frequency domain in real-time. The underlying motivation is an increased distinguishability of signal and noise in frequency domain. A first experimental campaign in a non-clinical setting with 22 MeV protons highlighting various aspects of the lock-in technique is presented. Finally, its application to clinical beam energies based on experimental and *in-silico* data is outlined.

2. Materials and methods

The *ToF*, further on labeled as ToF^{BP}, is considered in this manuscript as the duration it takes for the IA wave to propagate from its source (Bragg peak) to the sensor surface and is therefore the most direct quantity to acoustically localize the Bragg peak maximum. In order to detect the ToF^{BP} of an IA signal buried in noise, the IA signal is modulated via the proton time profile. This so-called signal modulation (frequency modulation) was achieved by pulsing the proton beam in a defined way while signal detection (demodulation) was carried out by lock-in amplifiers on the basis of the continuously measured IA signal. The following sections outline the experimental study at 22 MeV (2.1), the demodulation methodology (2.2), the reference analysis including the simulation framework (2.3, 2.4) and lastly a digital lock-in on simulated and experimental IA signals both based on clinical proton beam energies (2.5).

2.1. Experimental study at 22 MeV
The experiments were carried out at the Tandem Van de Graaff accelerator of the MLL, LMU and TUM in Garching with pulsed 22 MeV proton beams. The following two subsections present the involved time signals and the experimental setup.

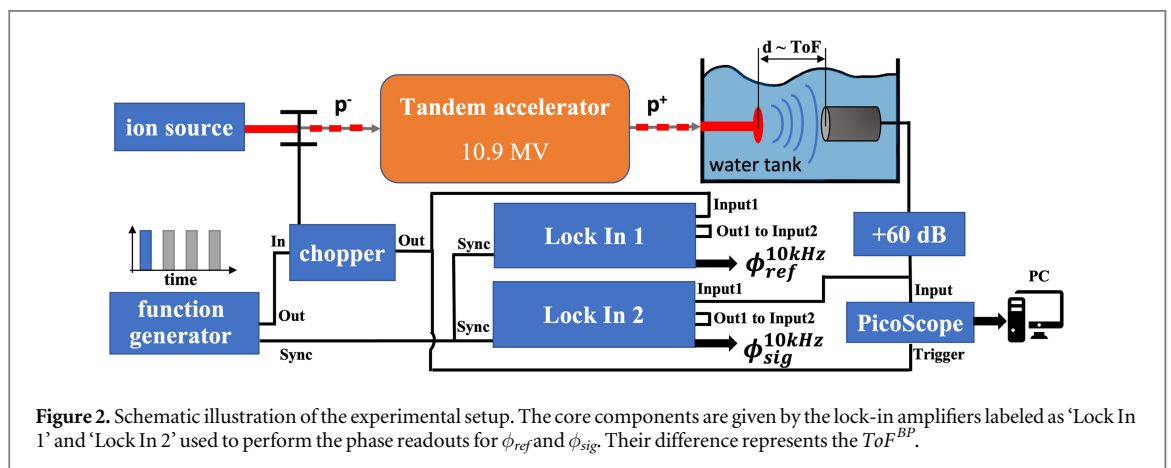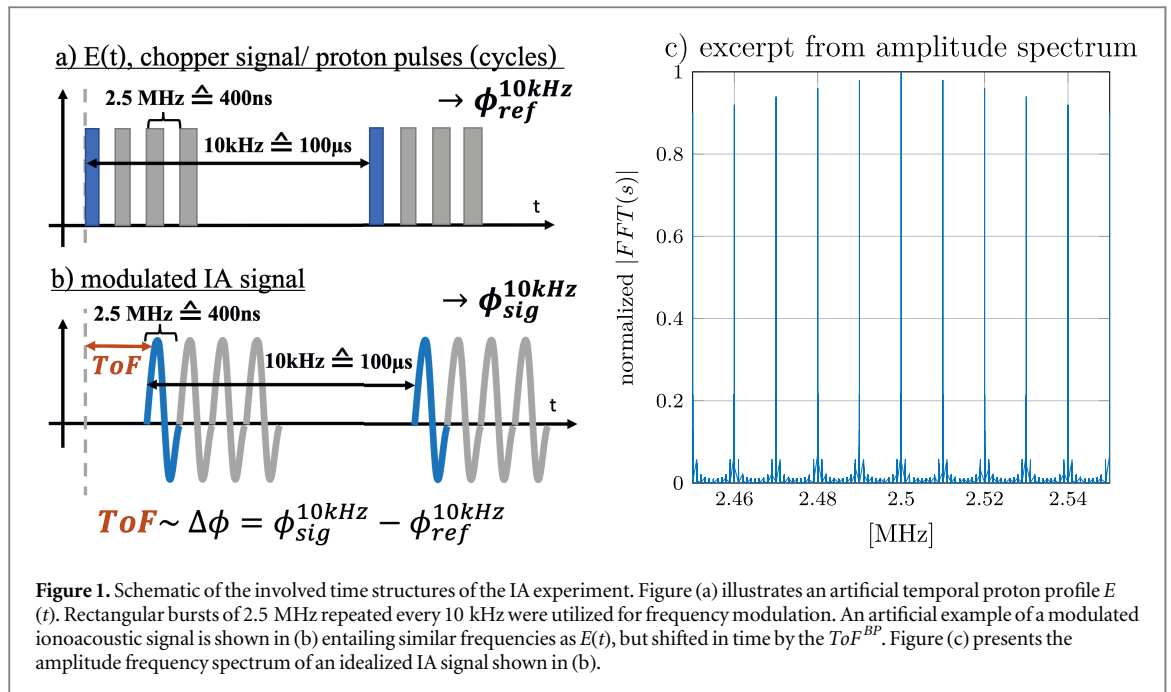#### 2.1.1. Frequency modulation and time structure of signals
High temporal gradients are beneficial for IA signal generation. Let $E(t)$ denote the proton pulse time profile and $P_\delta(\mathbf{r}, t)$ be the scaled spatial heating function seen by an idealized point detector at location $\mathbf{r}$ and time t, then the measured pressure $p(\mathbf{r}, t)$ is given by Jones *et al* (2016a):

$$p(\mathbf{r}, t) = \frac{\partial}{\partial t}[E(t) \circledast P_\delta(\mathbf{r}, t)] = \left[\frac{\partial E(t)}{\partial t} \circledast P_\delta(\mathbf{r}, t)\right]. \tag{1}$$

The second part of equation (1), namely $\frac{\partial E(t)}{\partial t}$ highlights the importance of high temporal gradients in the proton pulse profiles for IA signal generation. In this work, quasi-rectangular proton pulse profiles were employed entailing short rise/fall times of 15 ns. Not only temporal gradients of $E(t)$ but also the pulse width of $E(t)$ impacts the IA signal. For efficient IA signal generation, temporal frequencies of $E(t)$ need to be aligned with spatial frequencies of the Bragg peak encoded in P_δ, which mainly lie between 2 and 3 MHz in the considered 22 MeV experiment. It was shown in a previous study (Lehrack *et al* 2020) for a 20 MeV proton energy that a pulse width of 200 ns generated the highest IA signal amplitude due to its stress confinement relation (Wang and Wu 2012) which can be approximated in this axial transducer setup by the longitudinal Bragg peak width, expressed by its full-width-half-maximum (FWHM). Let the FWHM be 300 μm and the speed of sound in water be 1.5 mm μs^{-1}, then the stress confinement is given by: 200 ns $= \frac{300\ \mu m}{1.5\ mm\ \mu s^{-1}}$. Thus a proton pulse width of 200 ns was utilized which corresponds to a frequency of 2.5 MHz (50% duty cycle).

Figures 1(a) and (b) present schematically the involved time structures whereby figure 1(a) depicts the chopper signal and 1(b) the modulated IA signal. Focusing on the chopper signal in 1(a), a frequency burst at 2.5 MHz with varying number of cycles was defined in the function generator to chop the continuous proton beam. This process can be understood as frequency modulation, as 2.5 MHz is imprinted onto the IA signal. Additional cycles used for frequency modulation with a duty cycle of 50% are shown in gray. The time between consecutive bursts was set to 100 μs, corresponding to a repetition frequency of 10 kHz in order to avoid acoustic interference between subsequent IA bursts. From the signal shown in 1(a) a reference phase shift ϕ_{ref} with respect to an internal reference clock was measured through a lock-in amplifier.

The artificial IA signal in figure 1(b) modulated at 2.5 MHz exhibits a similar time structure compared to 1(a) with the main difference of being shifted in time (Dollinger *et al* 2016). As all protons stop in less than a few ns, this time-shift approximates the ToF^{BP}. Consequently, the time shift equals a phase shift ϕ_{sig} in frequency domain which is measured with a second lock-in amplifier, also synchronized to the same internal clock of the first lock-in amplifier. The phase difference $\Delta\phi = \phi_{sig} - \phi_{ref}$ then directly approximates the ToF^{BP}. The employed time profiles 2.5 MHz (=micro structure) with N cycles (=macro structure) repeating at 100 kHz

Figure 1. Schematic of the involved time structures of the IA experiment. Figure (a) illustrates an artificial temporal proton profile E (*t*). Rectangular bursts of 2.5 MHz repeated every 10 kHz were utilized for frequency modulation. An artificial example of a modulated ionoacoustic signal is shown in (b) entailing similar frequencies as $E(t)$, but shifted in time by the ToF^{BP}. Figure (c) presents the amplitude frequency spectrum of an idealized IA signal shown in (b).

Figure 2. Schematic illustration of the experimental setup. The core components are given by the lock-in amplifiers labeled as 'Lock In 1' and 'Lock In 2' used to perform the phase readouts for ϕ_{ref} and ϕ_{sig}. Their difference represents the ToF^{BP}.

differ from clinical synchrocyclotrons which typically reveal a finer micro structure from the acceleration radio frequency (>50 MHz). Moreover, the macro pulse structure amounts to approximately 10 μs ($\triangleq$ 100 kHz) repeating at 1 kHz. Figure 1(c) illustrates an excerpt of the normalized amplitude spectrum of idealized IA signals at 2.5 MHz repeated every 10 kHz. The signal amplitude is centered at 2.5 MHz and reveals characteristic sidebands at 2.5 MHz $\pm$ integer multiples of 10 kHz. The tandem lock-in analysis, explained later in section 2.2 is based on the sideband at 2.51 MHz.

2.1.2. Experimental hardware setup

A sketch of the experimental setup is illustrated in figure 2. A function generator (Rigol DG4162), operated in burst mode at the control room, was used to steer the chopper system cutting the continuous proton beam into user-defined proton pulses (Rohrer *et al* 1984). After acceleration and beam guidance to the experimental site, the proton bunches stopped in a water tank and revealed a maximum dose deposition at 4.88 mm (range R80 of 4.93 mm). The lateral spot size at the exit nozzle was quantified by a Gafchromic film measurement resulting in a lateral beam spread of $\sigma_{x,y} = 1.4$ mm. Because of (i) the low momentum spread of about ± 10 keV (Assmann *et al* 2015), (ii) the relatively low proton energy exhibiting minimal range straggling and (iii) the supporting temporal frequencies, the resulting IA signals were for an axial measurement configuration in the MHz range. A single element $0.5''$ in diameter spherically focused PZT transducer (Type V382-SU, OLYMPUS) with a central frequency of 3.5 MHz and a bandwidth of 72% at -6 dB was aligned on the beam axis distal to the Bragg peak to measure IA emissions. The Bragg peak to transducer distance, which is proportional to the ToF^{BP}, was about 5 cm. The transducer was connected via a short cable to a low noise voltage amplifier (LNA) of $+60$ dB

(HVA-10M-60-B, FEMTO, Messtechnik GmbH) and then fed into a digital oscilloscope (6404D PicoScope, Pico Technology Ltd.) to acquire triggered IA signals at 8 bit resolution using ± 50 mV range as reference. The oscilloscope was operated with a sampling time of 6.4 ns and data acquisition was triggered by the chopper signal.

The chopper output signal was connected via a ≈ 200 m cable to the PicoScope and to the first lock-in amplifier (HF2LI 50 MHz, Zurich Instruments) both located near the beam exit window. Additionally, the LNA's output (IA signal) was linked to the input of the second lock-in amplifier (UHFLI 600 MHz, Zurich Instruments). Both lock-in amplifiers were operated in master-slave mode to acquire the reference phase ϕ_{ref} and the signal phase shift ϕ_{sig} simultaneously. Their difference gave rise to the ToF^{BP}. To avoid phase drifts in the readout, the internal clocks of the function generator and lock-in amplifiers were synchronized. Alternatively, a single lock-in amplifier can also be employed if a calibration measurement is performed upfront.

Both lock-in amplifiers act as analog-to-digital converters (ADC) and online digital processing units. The total acquisition time for each measurement was 9 s using an ADC sampling frequency of 210 MHz. The lock-in amplifier's phase is measured in radians as a function of time with 14 bit resolution. The performed tandem demodulation which is explained later, required a cable bridge, labeled as 'Out1 to Input2' in figure 2, to link the two consecutive demodulations.

The average beam current considering 200 ns proton pulses repeated every 100 μs amounted to ≈ 5 nA ± 1.5 nA and was measured with a Faraday cup located right before the beam exit window yielding a charge per pulse of 0.5 pC (3.2×10^6 particles per pulse). This corresponds to a maximum dose deposition at the Bragg peak of 0.8 Gy per pulse and induced a peak pressure of about 80 Pa.

We decided to use the chopper signal for stability reasons as a surrogate for the arrival of protons in the water tank. Therefore, we measured upfront in a separate experiment the time offset between the chopper signal and the actual proton arrival at the experimental site. To quantify this systematic temporal offset (interplay of cable length delays and accelerator specific time lags), a thin and fast silicon detector (Tran *et al* 2015a, 2015b) was connected together with the chopper signal to a 4GHz oscilloscope (LeCroy Wave Runner 640Zi, Teledyne LeCroy, USA) using a sampling time of 50 ps. We found for this experimental condition at 22 MeV a systematic delay of $t_{offset}^{chop} = -1.43$ μs indicating the chopper signal measured at the experimental site arrived 1.43 μs before the protons. This offset is then accounted for in the data analysis. In addition, the measured pulse profiles were deconvoluted with the detector's impulse response (Würl *et al* 2018) to determine the proton pulse widths from 40 ns to 2000 ns. A mean error of less than 4 ns between the specified pulse widths at the function generator and measured pulse widths could be observed herewith indicating good agreement.
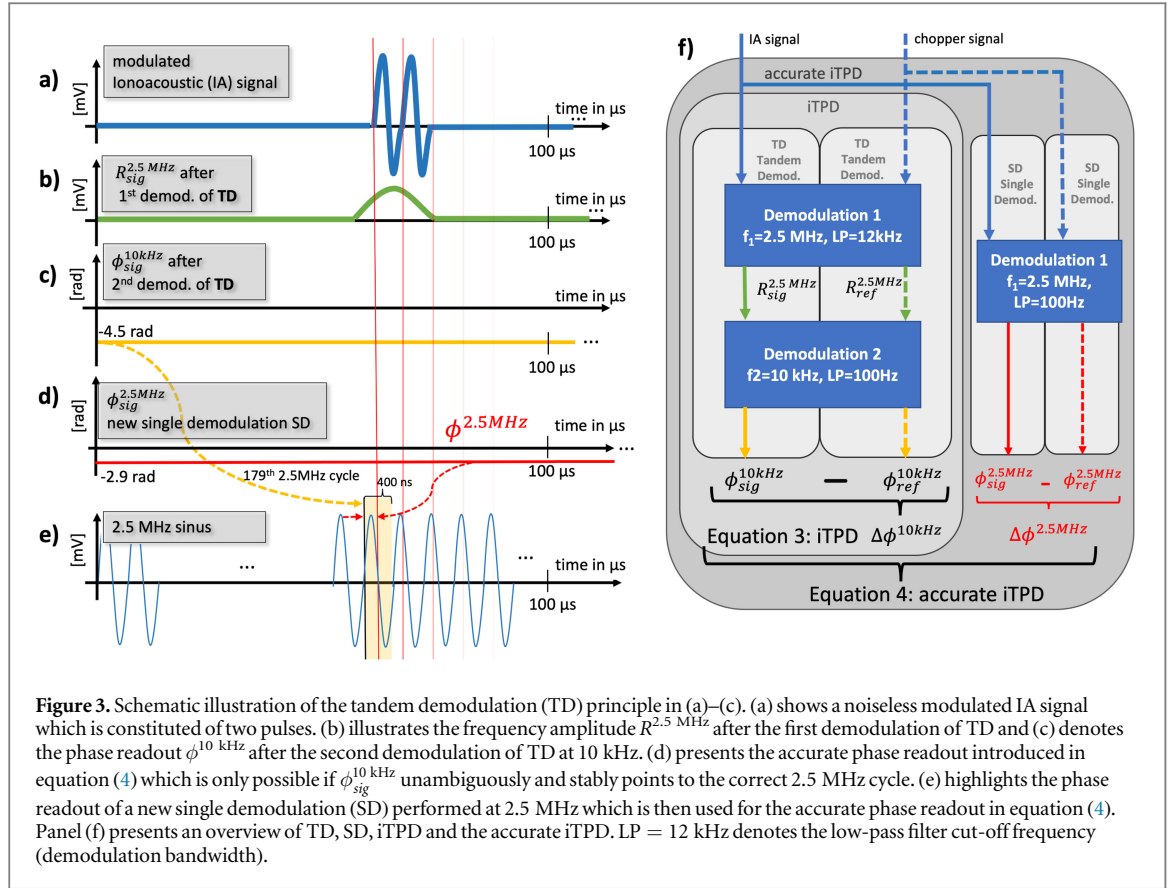
2.2. Demodulation method

A lock-in amplifier performs a homodyne signal detection which means that modulation and demodulation are performed at the exact same frequency. The lock-in amplifier acts as a narrow band-pass filter which is realized by a two-step process of signal mixing and low-pass filtering. This process is called demodulation and is explained in appendix A.

2.2.1. Tandem demodulation

Two consecutive demodulations form a so-called tandem demodulation (TD) and its functional principle is illustrated in figure 3. The first signal in figure 3 mimics the IA signal which is comprised of two acoustic pulses of 2.5 MHz repeated every 100 μs as an example. Thus, the modulation frequencies from the proton time profile were 2.5 MHz and 10 kHz.

During tandem demodulation (TD), the measured IA signal is demodulated twice. In the first demodulation at $f_{1,ref} = 2.5$ MHz the output amplitude $R^{2.5 \text{ MHz}}$ is obtained, which is shown in figure 3(b) by the green solid line. The demodulated amplitude peaks when a 2.5 MHz signal is present and becomes zeros otherwise. Therefore, the first demodulation can be understood as IA signal detection. However, since $R^{2.5 \text{ MHz}}$ peaks every 10 kHz due to the pulse repetition rate, a second demodulation can be carried out. For this, $R^{2.5 \text{ MHz}}$ is fed into a second demodulation (cable bridge Out1 to Input2 in figure 2), this time at $f_{2,ref} = 10$ kHz, to find the occurrence of 2.5 MHz frequencies within the 10 kHz phase. The output phase of the second demodulation $\phi^{10 \text{ kHz}}$ represents the quantity of interest as it measures the 10 kHz phase of the IA signal compared to an internal reference. $\phi^{10 \text{ kHz}}$ is illustrated in figure 3(c) by the stable yellow line and denotes the final output of TD. The two demodulation frequencies of TD, i.e. 2.5 MHz and 10 kHz, were chosen based on prior knowledge of the proton beam time structure.

Each of the two lock-in amplifiers performed a TD in parallel. The first lock-in amplifier demodulated the chopper signal to obtain $\phi_{ref}^{10 \text{ kHz}}$ and the second lock-in amplifier demodulated the IA signal to derive $\phi_{sig}^{10 \text{ kHz}}$. Their relative phase difference $\Delta\phi^{10 \text{ kHz}}$ can then be used to derive the ToF^{BP} of the IA wave. This process is

Figure 3. Schematic illustration of the tandem demodulation (TD) principle in (a)–(c). (a) shows a noiseless modulated IA signal which is constituted of two pulses. (b) illustrates the frequency amplitude $R^{2.5\,\mathrm{MHz}}$ after the first demodulation of TD and (c) denotes the phase readout $\phi^{10\,\mathrm{kHz}}$ after the second demodulation of TD at 10 kHz. (d) presents the accurate phase readout introduced in equation (4) which is only possible if $\phi_{sig}^{10\,\mathrm{kHz}}$ unambiguously and stably points to the correct 2.5 MHz cycle. (e) highlights the phase readout of a new single demodulation (SD) performed at 2.5 MHz which is then used for the accurate phase readout in equation (4). Panel (f) presents an overview of TD, SD, iTPD and the accurate iTPD. LP = 12 kHz denotes the low-pass filter cut-off frequency (demodulation bandwidth).

labeled as ionoacoustic tandem phase detection (iTPD):

$$\Delta\phi^{10\,\mathrm{kHz}} = \phi_{sig}^{10\,\mathrm{kHz}}(R_{sig}^{2.5\,\mathrm{MHz}}) - \phi_{ref}^{10\,\mathrm{kHz}}(R_{ref}^{2.5\,\mathrm{MHz}}) \tag{2}$$

$$ToF_{exp} = \Delta\phi^{10\,\mathrm{kHz}}\frac{T^{10kHz}}{2\pi} + t_{offset}^{chop} + t_{offset}^{demod}, \tag{3}$$

where $R_{sig}^{2.5\,\mathrm{MHz}}$ and $R_{ref}^{2.5\,\mathrm{MHz}}$ are the amplitudes of the first demodulation at 2.5 MHz of the IA signal and the chopper signal. The expression $\phi^{10\,\mathrm{kHz}}(R^{2.5\,\mathrm{MHz}})$ highlights the linkage between the two consecutive demodulations as part of TD in which the phase $\phi^{10\,\mathrm{kHz}}$ of 10 kHz is a function of the demodulated signal amplitude $R^{2.5\,\mathrm{MHz}}$ at 2.5 MHz. Equation (3) approximates the ToF_{exp}. A more accurate formalism is introduced later. The subscript *exp* in ToF_{exp} indicates this quantity was derived from experimental measurements. t_{offset}^{chop} denotes the offset between chopper signal and proton arrival (1.43 μs) while t_{offset}^{demod} depicts a demodulation specific time offset which is explained in appendix B.

Converting $\Delta\phi^{10\,\mathrm{kHz}}$, which is measured in rad, to time considering a period of $T^{10\,\mathrm{kHz}} = 100\ \mu$s, allows inferring the *ToF* in a time window between between 0 and 100 μs $\pm$ integer multiplies of 100 μs. For example, measuring a phase difference of $\Delta\phi^{10\,\mathrm{kHz}} = -4.5$ rad indicates a ToF_{exp} of 71.62, 171.62, 271.62 μs, ... considering the 100 μs period of 10 kHz. The negative sign of the readout (-4.5 rad) indicates the signal arrives after the reference.

The phase readout of iTPD was defined as sufficiently stable when the progressive standard deviation $\sigma[\phi^{10\,\mathrm{kHz}}]$ fulfilled the following condition: $\sigma[\Delta\phi^{10\,\mathrm{kHz}}] < \frac{2\pi T^{2.5\,\mathrm{MHz}}}{T^{10\,\mathrm{kHz}}}$ given $T^{2.5\,\mathrm{MHz}}$ represents the period of 2.5 MHz. This criterion allows to unambiguously determine the current cycle of a continuous 2.5 MHz signal which can then be incorporated into a modified iTPD readout to achieve greater accuracy (Dollinger *et al* 2016). The phase readout of $\phi_{sig}^{2.5\,\mathrm{MHz}}$ allows only to measure a time between 0 and 0.4 μs and leads consequently to ambiguities in the 100 μs period as indicated by vertical red lines in figure 3. To identify the correct 2.5 MHz cycle, a stable $\phi_{sig}^{10\,\mathrm{kHz}}$ phase readout is required to pinpoint to the correct 2.5MHz cycle. This interconnection is illustrated by the dashed yellow arrow in figures 3(c), (e). Let $\lfloor \cdot \rceil$ be the operator rounding to the nearest integer, then an accurate *ToF* measurement can be achieved via:

$$ToF_{exp}^{acc} = \left(\left\lfloor \underbrace{\underbrace{ToF_{exp}}_{\text{iTPD,Eq3}} \frac{1}{T^{2.5\text{ MHz}}}}_{\#2.5\text{MHzcycles}} - \frac{\Delta\phi^{2.5\text{ MHz}}}{2\pi} \right\rceil + \frac{\Delta\phi^{2.5\text{ MHz}}}{2\pi} \right) T^{2.5\text{ MHz}}. \tag{4}$$

Equation (4) describes the accurate iTPD readout which additionally incorporates a new single demodulation (SD) at 2.5 MHz. The expression within $\lfloor \cdot \rceil$ denotes the number of 2.5 MHz cycles. Fluctuations of ToF_{exp} around $\pm T^{2.5\text{ MHz}}/2$ derived from TD do not influence the number of # 2.5 MHz cycles.

$\Delta\phi^{2.5\text{ MHz}}$ is obtained in similar fashion to $\Delta\phi^{10\text{ kHz}}$ (equation (2)) by subtracting $\phi_{sig}^{2.5\text{ MHz}}$ from a reference $\phi_{ref}^{2.5\text{ MHz}}$. An overview of TD, SD, iTPD, the accurate iTPD and their methodological interconnection is presented in figure 3(f).

Following the example in figure 3 and dividing the iTPD readout of 71.62 μs by the period of 0.4 μs results in 179.04 cycles. Applying the rounding operator yields to 179 complete 2.5 MHz cycles. For a continuous sinus wave at 2.5 MHz, the iTPD readout points to the 179th 2.5 MHz cycle which is highlighted by the yellow dashed arrow in figures 3(c), (e). Deriving the 2.5 MHz phase $\phi_{sig}^{2.5MHz}$ from a new separated single demodulation SD (see red dashed arrow in figure 3(d)) allows to exercise the remaining part of equation (4) which is $179 \cdot 0.4\ \mu\text{s} + \frac{2.9 \cdot 0.4\ \mu s}{2\pi} = 71.78\ \mu\text{s}$. If iTPD ($ToF_{exp}$) points to a wrong 2.5 MHz cycle, then the resulting error for the accurate iTPD can reach multiples of 0.4 μs. The experimental result of iTPD is shown in the result section 3.1.1.

An important aspect of iTPD are the low-pass filter parameters defining the bandwidth of each demodulation. Considering the amplitude spectrum in figure 1(c), a TD in the given scenario utilizes the signals at 2.5 MHz and the sideband at 2.51 MHz. The first demodulation shifts the frequency spectrum to 0 Hz (see also appendix A). The cut-off frequency of the low-pass filter of the first demodulation needs to be greater than the second demodulation frequency to not filter the content of interest beforehand. Therefore, the general rule for iTPD in this configuration is to use a low-pass filter in the first demodulation with a cut-off frequency greater than 10 kHz. For the experiments, a cut-off frequency at -3 dB of 12 kHz was employed for the first demodulation and 100 Hz for the second demodulation if not stated otherwise. The filter order for all low-pass filters was set to 3.

For the accurate phase readout $\Delta\phi^{2.5\text{ MHz}}$ it is advisable to not use the output of the first demodulation of iTPD which is employing a low pass filter of 12 kHz but instead perform a third new single demodulation (SD) at 2.5 MHz with a narrow low-pass at a few Hertz. This SD is presented in figure 3(f) by the outer right signal path to obtain $\Delta\phi^{2.5\text{ MHz}}$ highlighted in red.

2.2.2. Systematic lock-in study

This section presents an overview of different lock-in aspects which were investigated individually with pulsed 22 MeV protons.

Time to lock-in and dose: For clinical application, it is required to perform iTPD measurements at relevant dose levels, i.e. in reasonable short time. The SNR and hence the accuracy and precision of iTPD depend on the employed low-pass filter characteristics. A narrow filter bandwidth allows rejecting noise regions effectively to obtain a stable phase readout. However, at the cost of longer filter settling times (filter response times) which lead to extended acquisition times and ultimately to more accumulated dose. Hence, the low-pass filter defines a direct trade-off between SNR and accumulated dose. The results of various low-pass filter parameters are presented in section 3.1.2.

Number of cycles: Increasing the number of proton cycles while maintaining the instantaneous current $\hat{I}$ (charge per cycle) creates a stronger 2.5 MHz component in the IA signal and results in higher $R_{sig/ref}^{2.5\text{ MHz}}$ values. The influence of the number of proton cycles on the precision of the relative phase shift $\Delta\phi^{10\text{ kHz}}$ is presented in the result section 3.1.3.

Higher harmonics: Harmonics occur after the first demodulation at integer multiples of 10 kHz and allow to perform the second demodulation of iTPD at $f_{2,ref} = 20$ kHz or $f_{2,ref} = 30$ kHz without modifying the actual input signal (chopper or IA signal). For instance, a $\Delta\phi^{20\text{ kHz}} = \pi$ represents a *ToF* of 25 μs considering the 50 μs period of 20 kHz. Such demodulations at harmonics can be performed by (i) adjusting the cut-off frequency of the low-pass filter of the first demodulation to not filter out the sideband of interest and (ii) performing the second demodulation at the frequency of the respective harmonic. The demodulation result at different harmonics is presented in the result section 3.1.4.

Acoustic resonator: Encoding a discrete frequency in the IA signal can not only be done via time excitation but also by means of resonators. Takayanagi *et al* (2019, 2020) placed a spherical gold marker in the beam path using clinical proton energies which created distinct resonance frequencies in the simulated and experimentally measured IA signal. Encouraged by their idea, we placed an aluminum cylinder with a diameter of 3.9 mm into
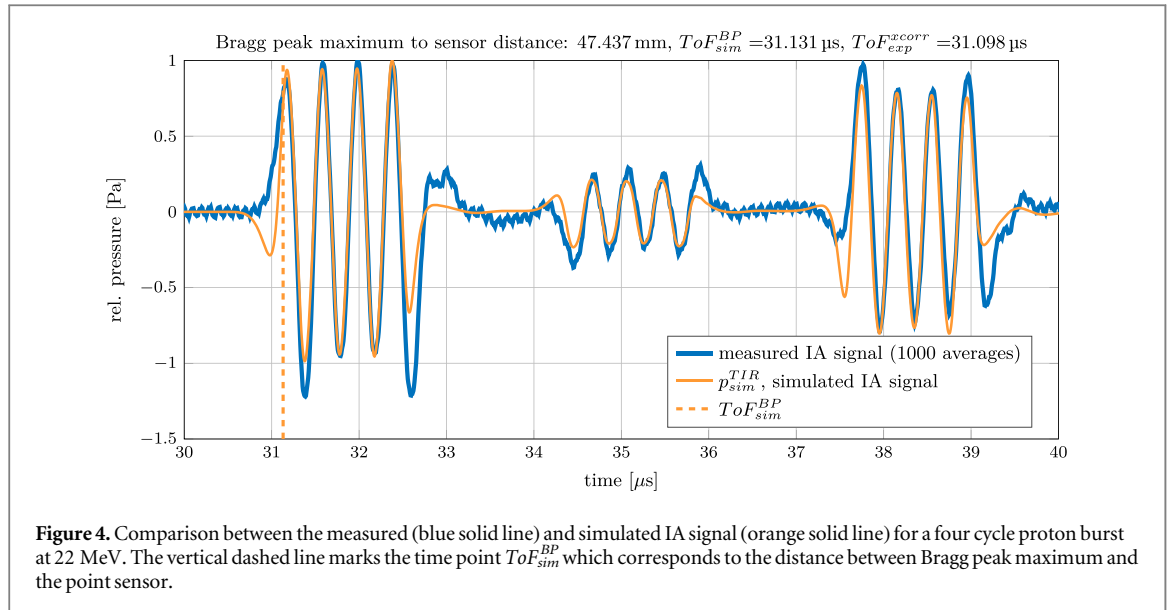
Figure 4. Comparison between the measured (blue solid line) and simulated IA signal (orange solid line) for a four cycle proton burst at 22 MeV. The vertical dashed line marks the time point ToF_{sim}^{BP} which corresponds to the distance between Bragg peak maximum and the point sensor.

the water tank experiment with 22 MeV protons. The cylinder axis was aligned perpendicular to the beam axis in the water tank and placed such that all protons stopped inside. The height of the cylinder was large compared to its diameter and the lateral beam dimensions. The aluminum cylinder was then irradiated with a single cycle proton burst at 2 MHz and distinct resonance frequencies were created. In addition to the IA signal acquisition with the PicoScope, an iTPD was performed with lock-in amplifiers. In this setting, iTPD was performed at 2.25 MHz and 10 kHz and the results are presented in the result section 3.1.5.

2.3. Reference method 1: cross-correlation

The measured ToF_{exp} via the relative phase shift in frequency domain (iTPD) is compared to a reference analysis utilizing cross-correlation to mimic the homodyne detection aspect of iTPD. The derived ToF from cross-correlating a 2.5 MHz sinus burst with the 1000-fold averaged IA signal, denoted as ToF_{exp}^{xcorr}, amounts to 31.098 μs and is outlined in appendix C.

2.4. Reference method 2: simulation framework

Two different dose deposition- and acoustic-simulation scenarios are presented next.

First, IA signals were simulated for 22 MeV protons stopping in water to emulate the experimental configuration described previously. From the simulated IA signal with known geometries, a reference ToF labeled as ToF_{sim}^{BP} was assessed in addition to ToF_{exp}^{xcorr}.

The second part of the *in-silico* studies focus on clinical energies. IA signals for 138 MeV protons targeting an artificial phantom were simulated considering an artificial heterogeneous geometry. The simulated IA signals are then fed into a digital lock-in analysis which is described in section 2.5.

2.4.1. 22 MeV protons—homogeneous setup

A simulation of the 22 MeV experiment has been carried out to derive a reference result which is not based on measured data. The simulation framework is explained in appendix D. A comparison of the measured and simulated IA signal p_{sim}^{TIR} is presented in figure 4.

A simulated IA signal with a maximum Bragg peak to sensor distance of 47.437 mm matched best with the averaged IA measurement taking into account experimental specific systematic time offsets. Considering the derived Bragg peak maximum to point sensor distance of 47.437 mm and a speed of sound at 37.1 °C (according to the experimental conditions) of 1.524 mm μs^{-1} yields a ToF_{sim}^{BP} of 31.131 μs which is highlighted by the vertical dashed orange line in figure 4. The small discrepancies between ToF_{sim}^{BP} and ToF_{exp}^{xcorr} are explained in appendices D and E. Both, ToF_{sim}^{BP} and ToF_{exp}^{xcorr} will be considered to benchmark lock-in measurements $ToF_{exp}/ToF_{exp}^{acc}$.

2.4.2. 138 MeV protons—heterogeneous setup

We expanded our *in-silico* study to a more realistic toy example emulating heterogeneities. The matRad toolkit (Wieser *et al* 2017) was used to simulate the dose deposition of a generic 138 MeV proton beam stopping in an artificial heterogeneous geometry. The proton beam was directed through a bone surrogate (Hounsfield Unit HU = 600) before stopping inside a target structure (HU=40). The surrounding phantom emulated water

(HU = 0). Acoustic and thermoacoustic properties were extrapolated from the HU values on the basis of look up tables provided in Jones *et al* (2018), Yu *et al* (2019). An idealized omnidirectional point sensor of infinite bandwidth was modeled and placed distal on the beam axis. The recorded pressure wave $p_{sim}^{\delta}(\boldsymbol{r_s}, t)$ was convoluted with a realistic clinical proton time profile from Lehrack *et al* (2017). No electrical transducer influences were modeled. In a final step, the simulated IA signal was fed into a digital iTPD which is described next.

2.5. Digital lock-in

The functionality of iTPD was implemented in a Matlab (MATLAB 2017) software program to perform a digital lock-in on simulated and experimental data in retrospect. One fundamental difference between triggered and lock-in measurements is their operation with continuous data streams. Therefore, individual IA signals from triggered acquisitions or simulations were extended to multiples of the pulse repetition frequency of the accelerator into a single continuous signal. The total duration of the synthetic signals was 1 s which corresponds to 1000 signals considering a realistic 1 kHz pulse repetition frequency.

First, a digital iTPD was carried out on an IA simulation (see section 2.4.2) considering 138 MeV protons stopping in an artificial heterogeneous geometry. Noise was added to the simulated pressure trace mimicking a similar SNR of -15 dB to Lehrack *et al* (2017). The signal was digitally demodulated at 35 and 3 kHz (third harmonic of 1 kHz) using low-pass filter bandwidths of $f_{-3\text{dB}}$ of 4500 Hz and of 10 Hz. The derived $ToF_{exp}/ToF_{exp}^{acc}$ were then compared to the obtained ToF_{sim}^{BP} from the simulation geometry (distance between transducer and Bragg peak maximum).

Second, experimental measurements from Lehrack *et al* (2017) were processed in the digital iTPD in retrospect. Lehrack *et al* (2017) irradiated a water tank with pulsed 220 MeV protons at the Center Antoine Lacassagne (CAL) in Nice, France. A hydrophone (Cetacean Research C305X, Seattle, USA) was utilized to measure IA emissions from a single proton cycle modulation in axial configuration. A Gaussian time profile with a FWHM of 4 μs was repeated every 1 ms (1 kHz). A window signal or reflections, as it was the case for 22 MeV, were not present in the IA signal because of the limited acquisition time. The first demodulation frequency was set to 25 kHz as the amplitude spectrum of the 1000-fold averaged IA signal peaked at this frequency. For the second demodulation, the third harmonic of 1 kHz was selected to derive $ToF_{exp}/ToF_{exp}^{acc}$. Further, we considered a low-pass filer cut-off frequency $f_{-3\text{dB}}$ of 4500 Hz for the first and 10 Hz for the second demodulation. The results are shown in section 3.2.2.

The clinical IA signal originating from a single cycle modulation contains a broad spectrum. Frequency components of about 50 kHz were observable in the compression (positive) pulse and 35–25 kHz in the rarefaction (negative) pulse. Since the latter is more pronounced in the Fourier domain, the IA signal was first demodulated at 35, 25 kHz, respectively. Consequently, iTPD measures the occurrence of 35, 25 kHz for which reason it needs to be known in advance how the demodulation frequency relates to ToF^{BP} corresponding to the Bragg peak maximum to sensor distance. Different demodulation frequencies result in different peak positions in the demodulation amplitude $R^{10-100\text{ kHz}}$ and hence different ToF_{exp} are derived via iTPD. Therefore, a time offset t_{offset}^{BP} was quantified for 25 kHz and 35 kHz from simulations and then subtracted from the digital iTPD readout (see equation (3)) to ensure the iTPD readout directly represents ToF^{BP}. A similar correction was required for the 22 MeV experiment, however, here a time offset t_{offset}^{BP} needed to be corrected due to additional acoustic reflections containing the demodulation frequency (see appendix B).
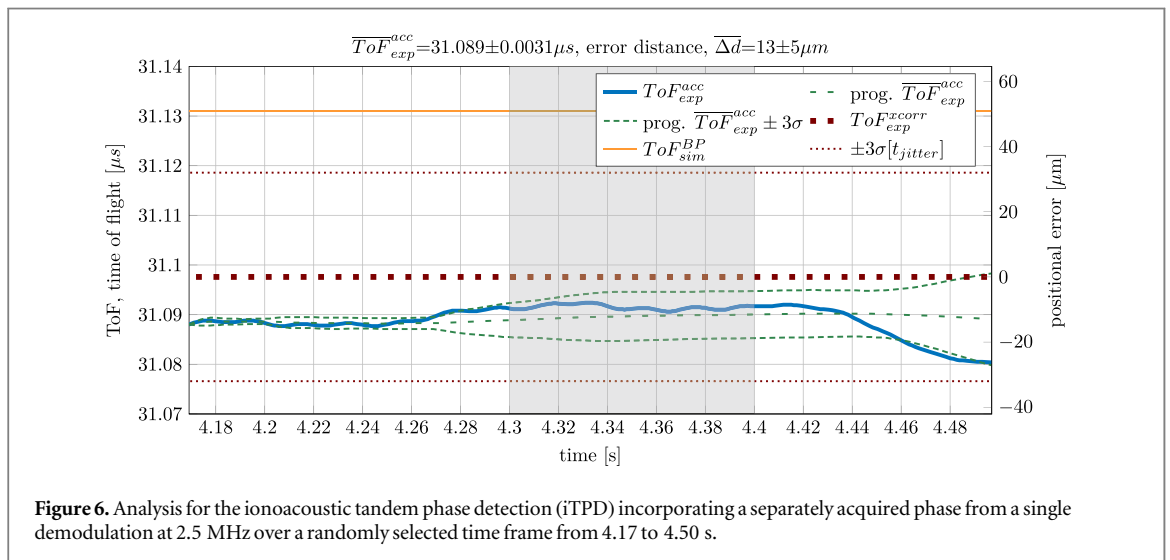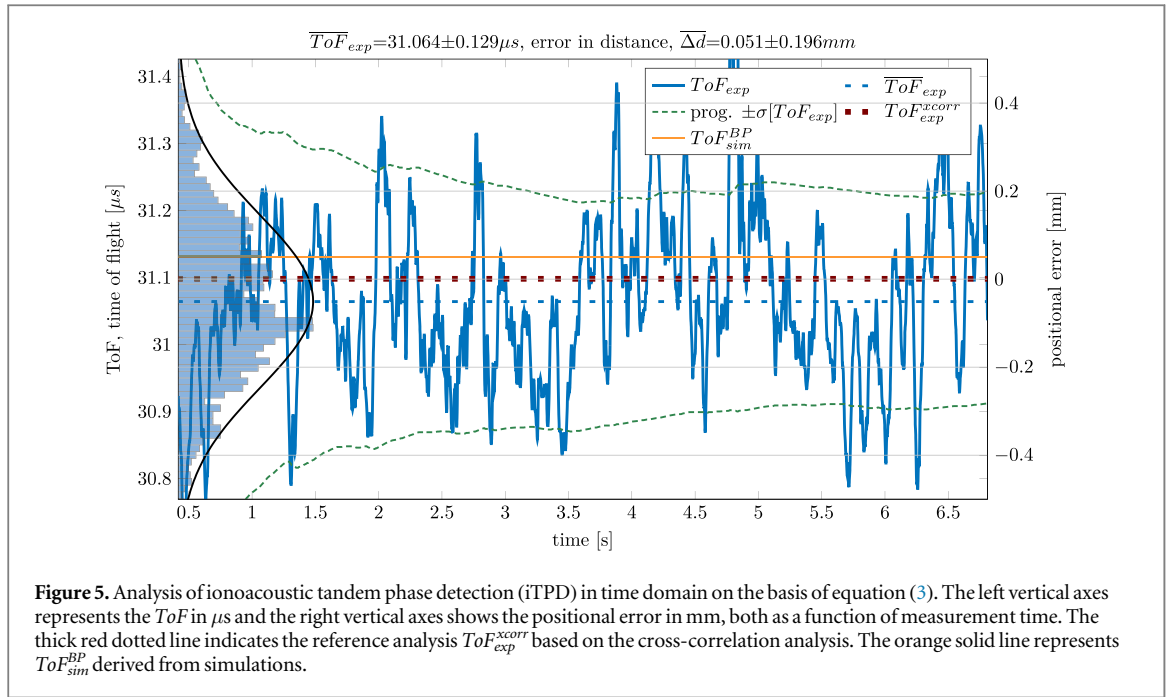
3. Results

3.1. iTPD at 22 MeV protons

The following results refer to the 22 MeV experiment described in section 2.1. An overview of the individual signals $\phi_{ref}^{10\text{ kHz}}$ and $\phi_{sig}^{10\text{ kHz}}$ over a time period of 9 s is given in appendix F while the resulting ToF_{exp} is presented next in section 3.1.1 considering a shorter time window.

3.1.1. iTPD versus accurate iTPD

The analysis of iTPD is shown in figure 5. The solid blue line in figure 5 presents the iTPD readout ToF_{exp} based on equation (3) over the measurement period of 0.5–6.8 s not yet incorporating the accurate phase readout. The histogram alongside a Gaussian fit to the experimentally measured ToF_{exp} over the measurement period is presented on the left vertical axis in figure 5. The mean $\overline{ToF_{exp}}$ amounts to 31.064 μs and deviates from $ToF_{exp}^{xcorr} = 31.098$ μs by 34 ns and is therefore within the uncertainty limit $\pm\sigma\,[ToF_{exp}]$ of 129 ns. The dashed blue line represents the mean $\overline{ToF_{exp}}$ while the dashed green line shows the progressive standard deviation $\pm\sigma\,[ToF_{exp}]$. The simulation result ToF_{sim}^{BP} is shown by the constant solid orange line.

Figure 5. Analysis of ionoacoustic tandem phase detection (iTPD) in time domain on the basis of equation (3). The left vertical axes represents the *ToF* in μs and the right vertical axes shows the positional error in mm, both as a function of measurement time. The thick red dotted line indicates the reference analysis ToF_{exp}^{xcorr} based on the cross-correlation analysis. The orange solid line represents ToF_{sim}^{BP} derived from simulations.

Figure 6. Analysis for the ionoacoustic tandem phase detection (iTPD) incorporating a separately acquired phase from a single demodulation at 2.5 MHz over a randomly selected time frame from 4.17 to 4.50 s.

The measured ToF_{exp} can be converted to distances using the speed of sound of water. The positional error, shown on the right vertical axis, was obtained by subtracting the distance obtained from ToF_{exp}^{xcorr} which is considered as reference. The reference, derived from ToF_{exp}^{xcorr}, is marked by the red dotted line, at 0 mm. The mean and standard deviation of the positional error amount to 51 $\mu m \pm 196$ μm. A Bragg peak sensor distance of 47.381 mm derived from ToF_{exp}^{xcorr} indicates a relative mean localization error for the homogeneous water tank measurements of 0.1% ($\frac{51\ \mu m}{47.381\ mm} * 100$).

Building upon figure 5, figure 6 presents the analysis including the accurate 2.5 MHz phase readout. However, it is important to stress that the 2.5 MHz phase can only be incorporated if its cycle can be determined unambiguously by iTPD. The respective time of flight, denoted as ToF_{exp}^{acc}, is shown by the blue solid line in figure 6 and amounts over the time window of 4.17–4.50 s to $\overline{ToF}_{exp}^{acc} = 31.089$ $\mu s \pm 0.003$ μs. The thick red dotted line highlights again $ToF_{exp}^{xcorr} = 31.098$ μs while the thin red dotted lines denote the jitter of $\pm 3\sigma = 21$ ns. From an analysis of individual IA measurements, a jitter/incoherence with a standard deviation of 7 ns could be observed from analyzing the peak variability from averaging randomly selected signal batches. Fifty randomly selected IA signals were pre-processed and averaged such that the acoustic peak position could be identified. This process was repeated 50 times to derive the variability of the IA signal separately.

The green dashed lines indicate the progressive mean (prog. $\overline{ToF}_{exp}^{acc}$) and standard deviation (prog. $\overline{ToF}_{exp}^{acc} \pm 3\sigma$). The latter reveals a value of 5 μm over the entire time window. Compared to figure 5, which does

Table 1. Accuracy and precision of different methods assessing the IA *ToF*. The detailed error estimation for ToF_{exp}^{xcorr} and ToF_{sim}^{BP} can be found in appendix G. The third column shows the deviation to ToF_{exp}^{xcorr} and fourth column the corresponding method of how this quantity was derived.

Quantity	Value	Deviation to ToF_{exp}^{xcorr}	Method
ToF_{exp}^{xcorr}	31.098 μs $\pm$ 9.8 ns	n.a.	Derived from cross-corr. (section 2.3)
ToF_{sim}^{BP}	31.131 μs $\pm$ 18 ns	33 ns	Derived from simulations (section 2.4)
ToF_{exp}	31.064 μs $\pm$ 129 ns	-34 ns	iTPD (equation (3))
ToF_{exp}^{acc}	31.089 μs $\pm$ 3.1 ns	-9 ns	Accurate iTPD (equation (4))

Table 2. Precision of tandem and single demodulation using varying number of cycles for the 2.5 MHz burst excitation.

		1 cycle	2 cycles	4 cycles	5 cycles
TD for iTPD (equation (3))	$\sigma[\phi]$ in [mrad]	56	54	9.9	9.1
	$\sigma[\phi]$ in [ns]	889	858	158	145
SD for acc. iTPD (equation (4))	$\sigma[\phi]$ in [mrad]	77	98	81.6	70
	$\sigma[\phi]$ in [ns]	5.5	7.0	5.7	5.0

not consider the additional 2.5 MHz phase information, the mean and standard deviation improved from 51 ± 196 μm to 13 ± 5 μm which now equals a relative localization accuracy and precision of $0.027 \pm 0.01\%$. Complementary, the right vertical axis of figure 6 illustrates the positional error with respect to ToF_{exp}^{xcorr} incorporating the dedicated 2.5 MHz phase readout. The grey box marks a time window of 100 ms which corresponds to the total acquisition time of 1000 IA signals considered to derive the reference ToF_{exp}^{xcorr}. Table 1 summarizes the different *ToF* quantities and their deviation to ToF_{exp}^{xcorr}. An error estimation of the standard deviation for ToF_{exp}^{xcorr} and ToF_{sim}^{BP} is given in appendix G. Differences between ToF_{sim}^{BP} and ToF_{exp}^{xcorr} of 33 ns can be explained by the fact that ToF_{sim}^{BP} is obtained from the distance between sensor and Bragg peak maximum as part of the simulation. As shown by Jones *et al* (2016a) ToF_{sim}^{BP} does not match with features of the recorded IA pressure such as the maximum value, zero crossing, or as in this case its correlation with a 2.5 MHz sinus burst. In the presented measurements, the systematic and intrinsic time difference between ToF_{sim}^{BP} and ToF_{exp}^{xcorr} amounts to 33 ns (50 μm). Comparing ToF_{exp}^{acc} to the simulation ToF_{sim}^{BP} results in a mean discrepancy of 42 ns. ToF_{exp}^{xcorr} and ToF_{exp}^{acc} were in figure 6 intentionally not corrected by their 33 ns, 42 ns offsets to emphasize their small differences. This aspect is further elaborated on in appendix E.

3.1.2. Time to lock-in and dose
The analysis for the settling time of the lock-in amplifier can be found in appendix H. The results showed a strong influence of the filter parameters on the required measurement time of iTPD and with that on the total accumulated dose. The time-based reference analysis ToF_{exp}^{xcorr} relied on 1000 individual proton bursts at 10 kHz which corresponds to an irradiation time of 100 ms. In contrast, the required lock-in time amounts according to table H1 to 9.1 ms.

3.1.3. Number of cycles
This section investigates the precision of iTPD considering various number of proton cycles while maintaining the instantaneous beam current $\hat{I}$. In the following, the number of proton cycles in the modulation was increased from 1 to 5 in order to progressively imprint a more pronounced 2.5 MHz component.

Table 2 shows the precision of TD (as part of equation (2)) in the two upper rows for different cycles. The standard deviation is given in mrad and ns and was calculated based on a measurement period of 9 s. Decreasing standard deviations can be observed for an increasing number of cycles for the given burst excitation. This indicates that encoding a stronger 2.5 MHz frequency in the IA signal by means of pulsing the beam, yields to an increased stability in iTPD. A significant improvement for TD could be observed between 2 and 4 cycles for which the standard deviation dropped from 858 ns to 158 ns.

The lower half of table 2 presents the standard deviation of a single demodulation at 2.5 MHz which is required as additional information for the accurate iTPD (as part of equation (4)). Here, an almost stable phase readout can be observed from table 2 across all cycles. $\sigma[\phi]$ varies for the 2.5 MHz phase readout only between 5 and 7 ns thereby indicating 2.5 MHz detection capabilities already for single cycle bursts. However this additional information can only be used if the 10 kHz phase readout of iTPD unambiguously points to the correct 2.5 MHz cycle.
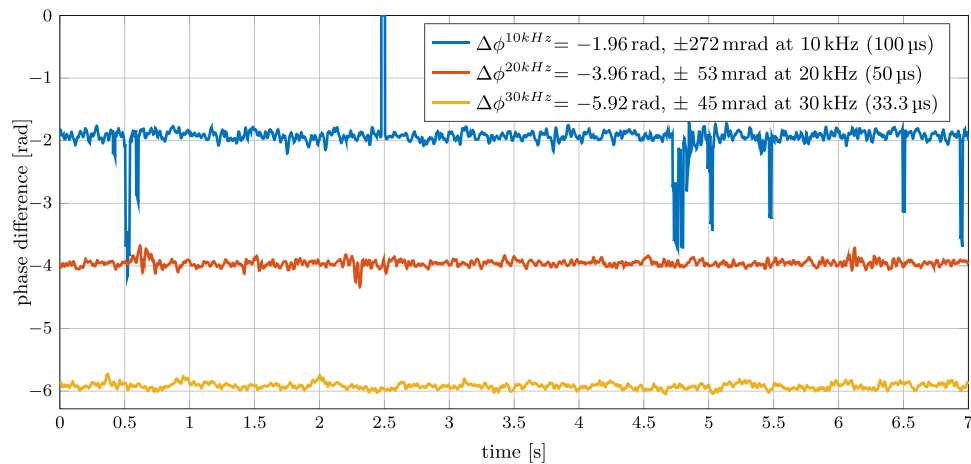
Figure 7. Analysis of TD utilizing a harmonic lock-in. A four cycled proton burst at 2.5 MHz was employed. The second demodulation as part of the tandem demodulation is performed at 10 kHz (blue line), 20 kHz (red line) and 30 kHz (yellow line).

For the results shown in table 2, the instantaneous beam current $\hat{I}$ (charge per cycle) was fixed which yields a linear increase of deposited dose. A five cycle burst deposits five times the dose of a single cycle excitation and hence, the DC beam current $\bar{I}$ increased by a factor of five.

The cut-off frequency of the low-pass filter parameter was set to 150 Hz for each measurement presented in table 2. Because of using a higher cut-off frequency in the low-pass filter in this investigation, the results in table 2 cannot be directly compared to section 3.1.1.

3.1.4. Lock-in on higher harmonics.
The previous results were based on carrying out the second demodulation as part of iTPD at 10 kHz. A Bragg-peak to transducer distance of 47.38 mm yielded a ToF_{exp}^{acc} of 31.089 μs, i.e. 1.95 rad. To make use of the additional 'free of charge' signal content at integer multiples, the second demodulation frequency of both lock-in amplifiers was subsequently changed from 10 kHz to 20 kHz and 30 kHz. To unambiguously derive the ToF_{exp}, the period of the second demodulation frequency must be greater than the ToF_{exp}. Both demodulations at 20 kHz and 30 kHz fulfilled this requirement as their periods amount to 50 μs and 33 μs, respectively. Performing the second demodulation at 20 kHz and 30 kHz increased the phase resolution because 50 μs and 33 μs were resolved over 0 rad to -6.238 rad for the price of decreasing frequency amplitudes of harmonics. It is important to stress that a harmonic lock-in does not require to change the proton burst excitation which was in this case still repeated every 10 kHz.

Figure 7 presents a comparison of the relative phase readout at 10, 20 and 30 kHz. A four-cycle rectangular burst of 2.5 MHz repeated every 10 kHz was utilized as proton time profile. Compared to the previous section, the low-pass filter of the second demodulation was changed to 200 Hz which explains the increased standard deviation of the $\Delta\phi^{10kHz}$ (solid blue line) compared to the previous analyses. Moreover, figure 7 presents iTPD without considering a dedicated 2.5 MHz readout.

From the reduced fluctuations in the readout in figure 7 it can be seen that performing the second demodulation at higher harmonics yields to a reduction of $\sigma[\Delta\phi]$ from 272 to 45 mrad. 272 mrad corresponds to 4.3 μs, 53 mrad to 420 ns and 45 mrad to 239 ns considering their respective periods. Consequently, a harmonic lock-in at 30 kHz allows to further consider the accurate 2.5 MHz phase readout to achieve greater accuracy as shown in the previous section 3.1.1.

3.1.5. Lock-in on a resonance frequency
As shown in section 3.1.3, increasing the number of cycles in burst excitation at the demodulation frequency is beneficial for the stability of iTPD. Nonetheless, imprinting a frequency in the IA signal can also be done by means of resonators. Here we investigate the impact of single pulse excitation on resonators using iTPD.

The measured and averaged IA signal with and without the cylindrical resonator are shown in time domain in figure 8(a). The blue solid line denotes the reference measurement without the cylindrical resonator revealing the well known triplet signature in the IA signal (direct, window and reflection). In contrast, the measurement with cylindrical resonator (red dotted line) shows a strongly oscillating IA signal with a steadily decreasing amplitude. Note that the transducer position and its distance to the Bragg peak is different compared to the previous measurements. Figure 8(b) shows the corresponding amplitude spectra. A pronounced signal content in the 1 MHz–2 MHz range can be observed due to the cylindrical resonator and the 2 MHz time excitation. The
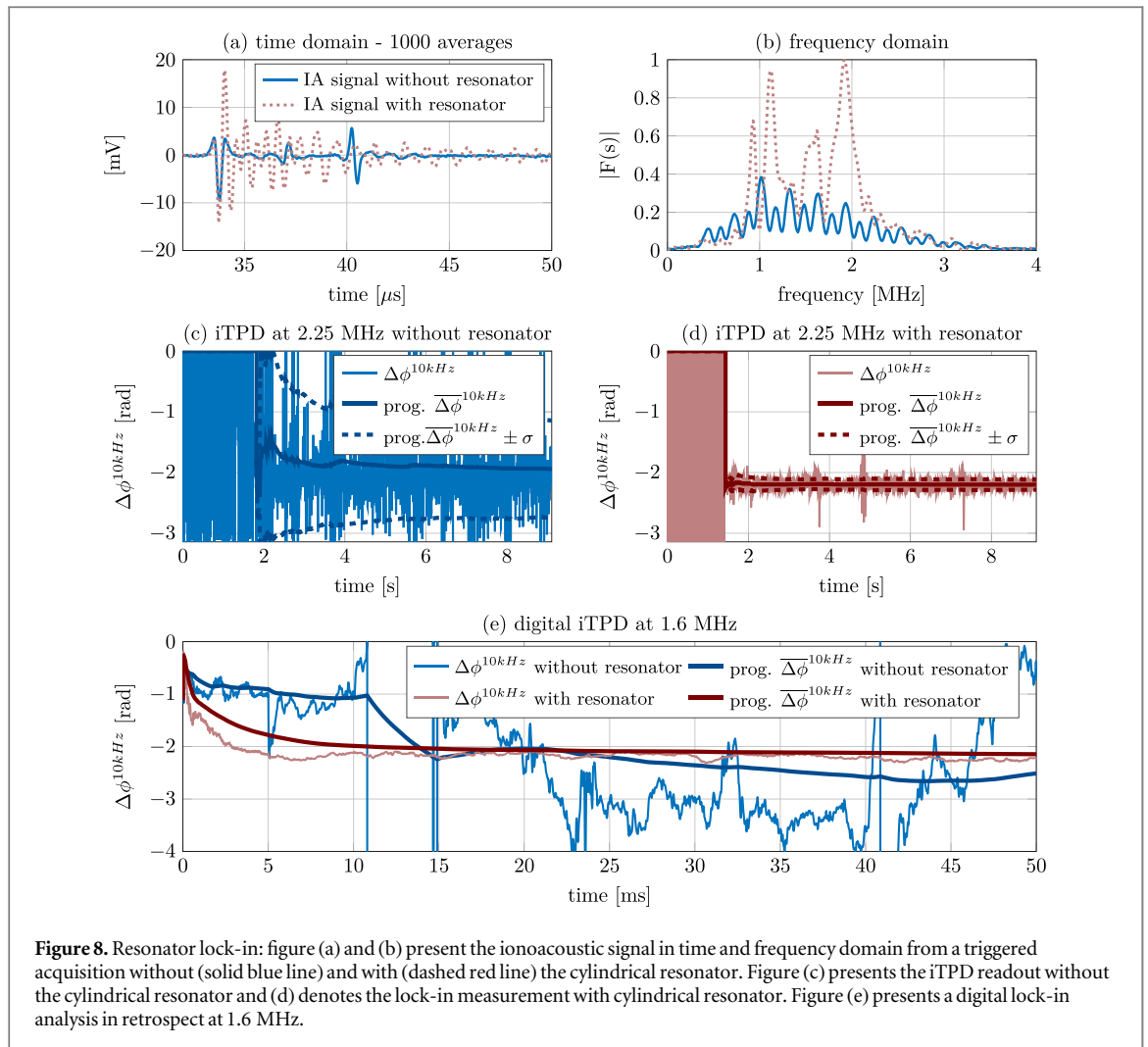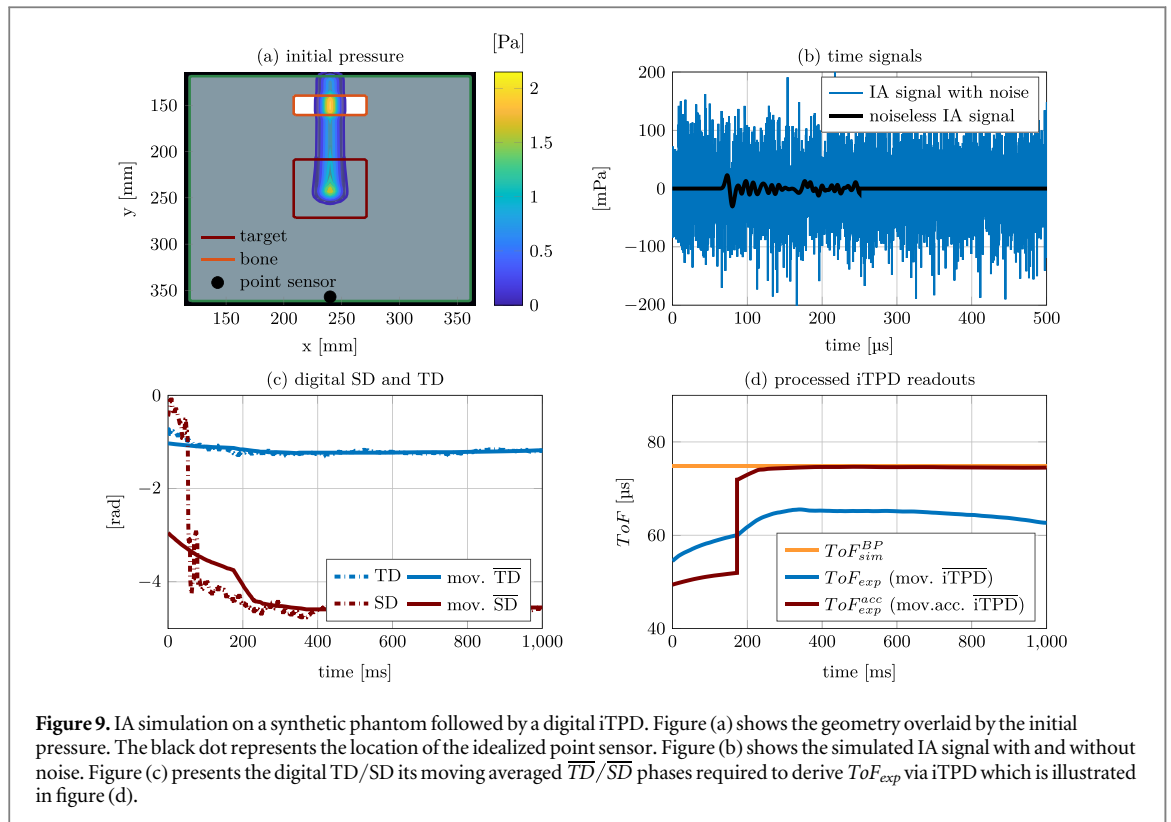
Figure 8. Resonator lock-in: figure (a) and (b) present the ionoacoustic signal in time and frequency domain from a triggered acquisition without (solid blue line) and with (dashed red line) the cylindrical resonator. Figure (c) presents the iTPD readout without the cylindrical resonator and (d) denotes the lock-in measurement with cylindrical resonator. Figure (e) presents a digital lock-in analysis in retrospect at 1.6 MHz.

2 MHz single cycle burst gives rise to the elevated peak in the amplitude spectrum at 2 MHz. The sound speed of aluminum ($c_{alu} = 6.250$ mm μs^{-1}) and the diameter of 3.9 mm result in a resonance frequency of 1.6 MHz which is observable in figure 8(b). Also a resonance frequency of 0.85 MHz corresponding to twice the diameter can be seen.

The experimental phase readout $\Delta\phi^{10kHz}$ in water without resonator is shown in figure 8(c) for which the beam was turned on after 1.8 s. The signal $\Delta\phi^{10kHz}$ strongly oscillates around -2 rad. The dark blue solid and dashed lines represent the progressive mean and standard deviation of $\Delta\phi^{10kHz}$. In contrast, figure 8(d) depicts the iTPD measurement for which protons stopped in the cylindrical resonator. In this measurement, the beam was turned on at 1.4 s. Comparing the standard deviations in figures 8(c) and (d) demonstrates the advantage of resonators for iTPD in an experimental setting.

It is to be noted that the Grüneisen parameter of aluminum is roughly 19 times higher compared to water and the acoustic transmission from aluminum to water is 30%. Assuming no transducer impulse response, this would theoretically yield a 6 times stronger signal amplitude for the cylindrical resonator measurement. However, the increased proton scattering in the aluminum, the different acoustic wave front due to the circular aluminum curvature as well as the -6 dB sensitivity level of the 3.5 MHz Olympus transducer at 2.2 MHz explain the reduced signal amplitude difference between these two measurements. Nevertheless, due to the aluminum cylinder acting as resonator at a distinct frequency and the increased signal amplitude, a more precise iTPD readout can be performed which is quantified by a decrease of $\sigma[\Delta\phi^{10kHz}]$ from 0.72 to 0.08 rad. Even though the lock-in frequency was not selected optimally (2.25 MHz instead of e.g. 1.6 MHz), the beneficial impact of resonators on iTPD is clearly demonstrated. Lastly figure 8(e) shows a digital lock-in performed in retrospect with the measured data, this time at the resonance frequency 1.6 MHz. Also in this analysis, the iTPD phase readout becomes more stable for the case of a resonance frequency. After 5 ms $\sigma[\Delta\phi^{10kHz}]$ drops from 1.05 to 0.05 rad when using a resonator. How resonators can be used for range verification is discussed in section 4.2.6.

Figure 9. IA simulation on a synthetic phantom followed by a digital iTPD. Figure (a) shows the geometry overlaid by the initial pressure. The black dot represents the location of the idealized point sensor. Figure (b) shows the simulated IA signal with and without noise. Figure (c) presents the digital TD/SD its moving averaged $\overline{TD}/\overline{SD}$ phases required to derive ToF_{exp} via iTPD which is illustrated in figure (d).

3.2. Digital lock-in on clinical beam energies

This subsection presents the results for the digital lock-in carried out on simulated and experimental IA signals in retrospect considering clinical beam energies.
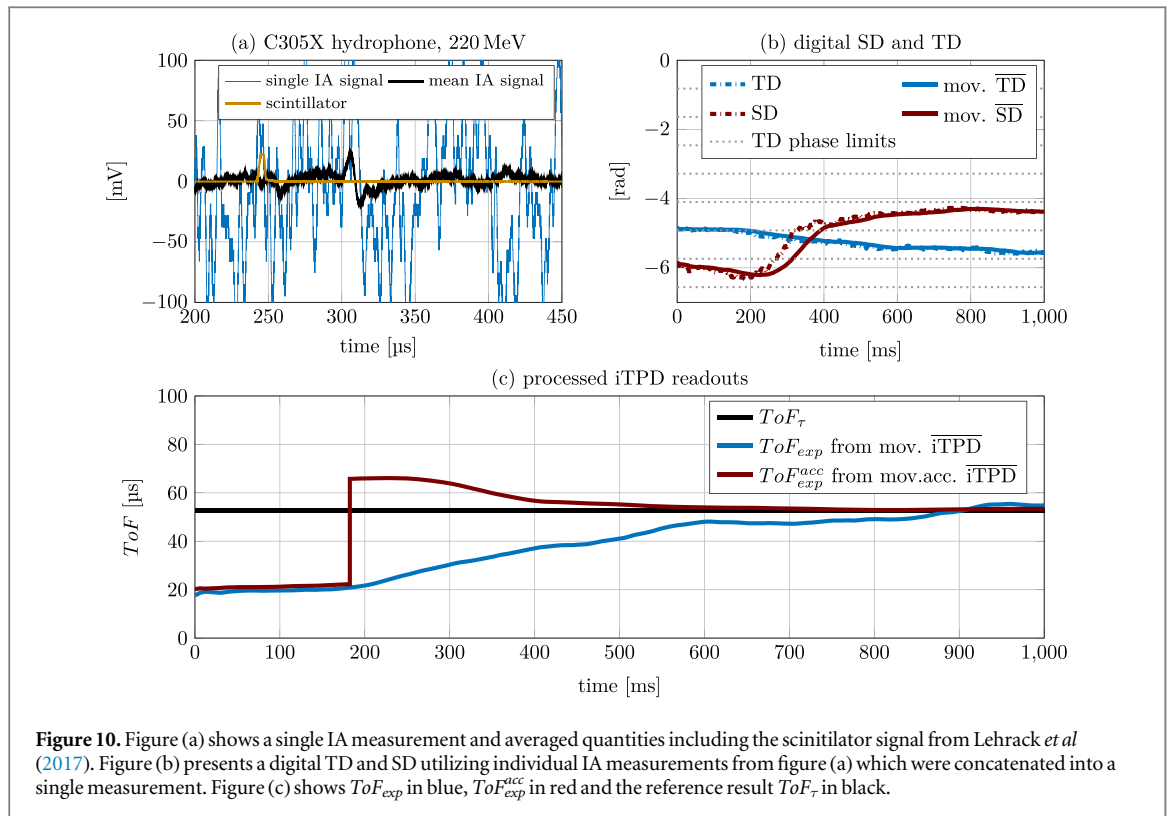
3.2.1. Artificial heterogeneous geometry

Figure 9 shows a digital iTPD on simulated IA signals on the basis of a generic 138 MeV proton beam stopping in an artificial heterogeneous geometry. The noiseless acoustic simulation result using the k-Wave toolbox is shown in figure 9(b) by the black solid line. Further, the blue line represents the noiseless IA signal overlaid by band-limited Gaussian noise. Next, 9(c) illustrates the raw readouts of TD (tandem demod.) and SD (single demod.) alongside their moving averages ($\overline{SD}$, $\overline{TD}$). Lastly, a digital $\overline{iTPD}$ was carried out to derive ToF_{exp} and ToF_{exp}^{acc} which are presented in 9(d).

As all material properties and the exact geometrical setup were known in the simulation, a ground truth ToF_{sim}^{BP} could be derived. Finally, ToF_{sim}^{BP} amounted to 74.81 μs and a mean ToF_{exp}^{acc} after 400 ms to 74.57 μs exhibiting a deviation of 72 ns, 0.1 mm respectively. 10 mGy maximum dose at the Bragg peak yields to 1.71 Pa initial pressure and to a measured pressure amplitude on the beam axis for an idealized point sensor 10 cm away of about 30 mPa. Summarized, lock-in times of less than 300 ms corresponding to 3 Gy were observed.

3.2.2. Experimental data at 220 MeV

The results of a digital lock-in on measured data are shown in figure 10. Firstly, figure 10(a) shows the experimental data from Lehrack *et al* (2017). The blue line presents one triggered IA measurement acquired with the hydrophone. The orange line depicts the averaged and inverted prompt gamma ray signal measured with a fast plastic scintillator (Bicron BC400 R, 4.5 cm) lateral to the beam axis. The black line shows the 1000-fold averaged IA signal where the Bragg peak signal near 300 μs can be separated from noise. The scintillator and IA signal were input into a digital lock-in amplifier to derive the *ToF* via iTPD. Figure 10(b) depicts the raw and moving-averaged readout of tandem demodulation (TD) and the additional single demodulation (SD) to perform the accurate iTPD. Because of fluctuation in the SD and TD readout, the moving averages ($\overline{SD}$, $\overline{TD}$) were calculated and further considered to derive the ToF_{exp} and ToF_{exp}^{acc} from $\overline{iTPD}$. The overline symbol indicates the consideration of moving averaged quantities. A lock-in on the 3rd harmonic at 3 kHz was performed as the signal arrives before 333.33 μs. The light blue dotted horizontal lines indicate different 25 kHz cycles, (40 μs periods). Note that, TD needs to stay within one cycle (between two dotted lines) to correctly incorporate the SD readout.

Figure 10. Figure (a) shows a single IA measurement and averaged quantities including the scinitilator signal from Lehrack *et al* (2017). Figure (b) presents a digital TD and SD utilizing individual IA measurements from figure (a) which were concatenated into a single measurement. Figure (c) shows ToF_{exp} in blue, ToF_{exp}^{acc} in red and the reference result ToF_{τ} in black.

The vertical black line in figure 10(c) presents the reference result ToF_{τ} extracted from averaged signals in 10(a) according to Lehrack *et al* (2017). The blue signal presents the ToF_{exp} converted from rad to μs accounting for the reference TD phase readout from the scintillator signal. After 600 ms the signal approximates the reference result ToF_{τ}. Incorporating $\overline{SD}$ for the accurate $\overline{iTPD}$ results in the red solid line in 10(c). Due to the rounding operator in equation (4), a step-like behavior can be observed. Once the correct 25 kHz cycle is identified via $\overline{iTPD}$ the accurate $\overline{SD}$ phase readout yields a precision of ± 0.31 μs which corresponds to ± 0.46 mm.

The deviation to ToF_{τ} amounts on average to 0.32 μs indicating reasonable agreement to the time based reference ToF_{τ} extracted from Lehrack *et al* (2017). It has to be noted that ToF_{τ} was derived from the time difference between the maximum IA signal and the 50% level of the scintillator signal. This procedure might not accurately represent the actual distance between hydrophone and Bragg peak maximum for which reason small discrepancies can be expected.

Considering the 1 ms pulse repetition rate and a Bragg peak dose of 10 mGy per pulse, the total time span of 500 ms corresponds to 500 pulses and a total peak dose of 5 Gy.

4. Discussion

4.1. General remarks

Unlike other domains like optoacoustics employing the lock-in technique to detect a modulated signal buried in noise, IA for clinical range verification is challenged with limited dosage because of clinical dose prescriptions. Typically, a lock-in amplifier demodulates a low-amplitude signal that is not limited in energy (dose) using a narrow low-pass filter to detect how strong the underlying source is emitting (Mascarenhas *et al* 1984). In contrast, this manuscript focuses on determining *ToF* from a phase shift at limited dosage to localize the emitting source.

Based on the frequencies encoded in the proton time profile, a tandem demodulation (TD) was performed at these frequencies to measure the relative phase between a known reference (chopper signal) and the IA signal. If TD is stable enough to uniquely identify the correct cycle of the first demodulation, then a new single demodulation (SD) can be incorporated in the phase readout to achieve greater accuracy and precision for measuring the *ToF*. Although not presented, the amplitude of SD/TD quantifies how strong the frequency is present in the IA signal and could in the future be used for dosimetric applications.

Besides measuring the *ToF* in real-time, a desirable aspect of lock-in amplifiers is the observed localization precision of frequencies in time domain resulting in a positional accuracy of 0.027% (13 μm) for the considered low proton energy and high frequency scenario. These results for 22 MeV protons were compared to a cross-correlation analysis utilizing 1000 triggered acquisitions exhibiting an iTPD accuracy and precision below 15 μm. Despite the large doses being applied in the experimental study for 22 MeV, the application of iTPD to clinical beam energies could be demonstrated for fractionated dose levels but still requires further improvements to reduce the integral dose.

4.2. Aspects of the iTPD method

4.2.1. Time-of-flight (ToF)

Comparing iTPD results to simulations, a mean difference in accuracy of 42 ns, 64 μm, respectively was observed. This difference is caused by the fact that each reference method ToF_{sim}^{BP} and ToF_{exp}^{xcorr} quantifies slightly different time points in the pressure wave. The general problem of deriving ToF^{BP} (see appendix E) from a measured IA signal is described in Jones *et al* (2016a) and depends among others, on the time profile, the sensor position and sensor orientation to the IA wave-front. Therefore, the actual Bragg peak to sensor distance corresponds in this setting to a time point before the first compression peak as part of the IA signal (see figures 4 and E1) which is also in line with observations from simulations. The cross-correlation analysis ToF_{exp}^{xcorr} presented in figure C1 quantified the time shift of a 2.5 MHz sinus burst (template). In detail, the computed ToF_{exp}^{xcorr} refers to the starting point (first positive non-zero value) of the utilized 2.5 MHz sinus burst (see appendix E). We recognize this intrinsic systematic difference between ToF_{sim}^{BP} and ToF_{exp}^{xcorr} which corresponds to a systematic offset.

4.2.2. Demodulation offset

The demodulation offset tackles the question how the demodulation frequency relates to the time point of interest (*ToF*). This aspect can be broken down into two cases—single and multiple IA pulses.

For single cycle excitation, e.g. at 2.5 MHz, it needs to be known, how a 2.5 MHz demodulation relates to the *ToF*. This imprecise knowledge is small for 2.5 MHz but becomes more pronounced for clinical beam energies for which the demodulation is done at much lower frequencies. A systematic time correction was required for the digital iTPDs performed for the clinical scenario presented in figures 9 and 10 both based on single pulse excitation. Here, the peak in the amplitude spectrum (35 kHz, 25 kHz respectively) was utilized as demodulation frequency corresponding to the rarefaction pulse. The association about when this frequency occurs (time-frequency relation) with respect to the *ToF* needs to be known *a priori* e.g. from an acoustic simulation or a calibration measurement.

The second scenario concerns multiple IA pulses (see appendix B). A systematic time offset in the demodulated 10 kHz phase was observed in the raw iTPD readout considering IA signals from pulsed 22 MeV protons. This offset occurs in the first 2.5 MHz demodulation due to acoustic reflections entailing the demodulation frequency at various time points. As a result, the demodulated amplitude peaked at the window signal and required a temporal correction by incorporating prior knowledge of the setup.

Considering clinical scenarios, the influence of a window or a reflection signal from the Bragg peak on the demodulation will be mitigated because of larger ranges resulting in stronger acoustic attenuation and weaker reflections, however, heterogeneities might induce additional signals at the demodulation frequency. One way to mitigate such effects is the application of a periodic windowing function to attenuate unwanted reflections. A expected time window can be approximated from the planned Bragg peak position and planned sensor location.

4.2.3. Frequency modulation—number of cycles

Increasing the number of cycles in burst excitation yielded an increased Bragg peak localization precision. In the experimental setup, the charge per cycle (instantaneous current $\hat{I}$) was kept constant resulting in a linear increase of dose (DC current $\bar{I}$) for increasing cycles. A four cycle burst deposited four times the dose of a single cycle burst herewith potentially violating clinical dose constraints.

The aspect of using bursts with varying number of cycles while ensuring constant dosage (const. $\bar{I}$ and varying $\hat{I}$) was not investigated experimentally with protons, but with synthetic signals from a function generator directly connected to lock-in amplifiers. Here, a four-cycle burst, entailed one fourth the signal amplitude $\hat{I}/4$ of a single cycle burst. No significant difference in the stability of the iTPD readout could be observed for increasing the number of cycles from 1 to 16 while simultaneously decreasing the signal amplitude to ensure integral signal energy (dose). Thus, increasing $\hat{I}$ while keeping $\bar{I}$ constant does not impact the stability of the lock-in readout. Hence, lock-in detection does not require high instantaneous beam currents $\hat{I}$ compared

to signal averaging. Low instantaneous beam currents $\hat{I}$, e.g. due to technical limits, require intensive signal averaging which becomes ineffective for large N as the noise level is proportional to the square root of N. In such low SNR conditions, especially due to limited $\hat{I}$, narrow band lock-in detection surpasses signal averaging.

Another noteworthy aspect is the phase stability of TD and SD. A single cycle experiment at 22 MeV produced for TD a precision of 889 ns. In contrast, SD exhibited a standard deviation below 7 ns across all cycles demonstrating SD is generally more stable than TD.

Considering clinical beam energies, a SD might be sufficient if prior knowledge is incorporated from the treatment plan. In the same fashion as TD, the correct SD cycle can alternatively be estimated from the planned Bragg peak location and sensor position. For example, assuming a Bragg peak to sensor distance of about 80 mm and a SD at 30 kHz ($T^{30\text{ kHz}} = 33\ \mu s$) which corresponds to a distance in water of 50 mm. It only needs to be known from treatment planning that the expected actual Bragg peak to sensor distance lies between 50 and 100 mm, which then corresponds to the second 30 kHz cycle. The accurate readout on a sub-millimeter level can then directly be performed using SD.

Another way of frequency modulation besides increasing the number of cycles is given by amplitude modulation, which can directly be applied in today's medical facilities using intensity modulated particle beams.

4.2.4. Time to lock-in

Another important aspect when considering integral dose limits is the time it takes for the lock-in amplifier to settle (speed of convergence). The settling time depends on the low-pass filter parameters. Narrow low-pass filters yield to stable readouts but long settling times and hence more accumulated dose over time. Contrary, higher SNR ratios allow the definition of relaxed filter bandwidths to achieve faster lock-in times. This study verifies the theoretical settling times of the utilized $f_{-3\text{dB}}$ of 10 and 100 Hz which amount to 100, and and 10 μs respectively.

The filter order and the cut-off frequency need to be optimized to the given experimental condition (SNR level). One approach for finding a better trade-off is given by reverse engineering the problem, where the prescribed dose and the dose per cycle defines the acquisition length which ultimately defines the optimal $f_{-3\text{dB}}$ cut-off frequency.

The large integral doses from the 22 MeV experiments exceed the clinical dose levels by two orders of magnitude. Since different lock-in amplifier aspects were systematically investigated in this first study, the applied dose was of lower importance. Considering a previous experimental IA measurement at a clinical synchrocyclotron facility (Lehrack *et al* 2017), the time structure of the IA signal is composed of a $\approx$25 kHz component repeated every 1 ms. As the clinical pulse repetition period of 1 ms is lower than the one used in the 22 MeV proton experiment (10 kHz), identical filter parameters result in a lower integral dose for the clinical case. Instead of kGy the required dose drops below 5 Gy motivating further exploration of iTPD for real time proton range verification.

4.2.5. Harmonic lock-in

The sidebands induced by the pulse repetition frequency allowed performing the second demodulation of iTPD at higher harmonics (20 kHz, 30 kHz) for the 22 MeV experiment without changing the proton burst repetition frequency of 10 kHz. To avoid ambiguities, the *ToF* to be measured needs to be smaller than the period of 20 or 30 kHz. As this was the case, a harmonic lock-in was performed exhibiting a decreased standard deviation of the phase $\sigma[\Delta\phi]$ for higher harmonics.

Despite the decreasing amplitude spectrum of higher harmonics, a reduced $\sigma[\Delta\phi]$ was measured. This can be explained by the increased phase resolution of 20/30 kHz and the demodulation at higher frequencies herewith moving away from the low-frequency $1/f$ noise. These two effects seem to outweigh the progressively decreasing signal amplitude of harmonics.

A reduced $\sigma[\Delta\phi]$ from a harmonic lock-in can enable accurate iTPD which incorporates a new third SD (see figure 6) to achieve greater Bragg peak localization accuracy and precision. Further, for a clinical synchrocyclotron with a pulse repetition rate of 1 kHz a harmonic lock-in at 2 or 3 kHz was feasible and allowed to measure *ToFs* of up to 500 and 333.3 μs as shown for the *in-silico* studies in the result section 3.2.

4.2.6. Acoustic resonator

Besides encoding a specific frequency via time excitation, also a resonator interacting with the ion beam can be used alternatively to create distinctive frequencies (Takayanagi *et al* 2019, 2020). A single cycle excitation caused resonance and resulted in an IA signal with distinct frequencies well suited for lock-in detection. One key advantage for clinical application of resonators compared to proton pulse modulation is the reduced dosage due to its single pulse excitation. Additional acoustic signals are not created by additional proton cycles but by the resonator itself.

Generally speaking, an energy density within a pair of strong acoustic interfaces such as water aluminum and aluminum water alongside a coherent and pronounced difference in the Grüneisen parameter induces a detectable resonance. Therefore the presence of metallic markers (Takayanagi *et al* 2019, 2020), solidified non-metallic markers (Rydhög *et al* 2017, Brown *et al* 2020) or contrast agents (Klein *et al* 2020, McNabb *et al* 2020, Lascaud *et al* 2021) might be suited for iTPD. Moreover, such resonances may also naturally appear in the human body, e.g. bony structures.

In the presented resonance study, the Bragg peak stopped within the aluminum resonator and the location of the resonator was effectively measured, however, for clinical range verification, incoming ions must traverse the marker/resonator to allow a relative Bragg peak localization to the marker. Focusing on the study of Takayanagi *et al* (2020), a lock-in amplifier can be used two-fold. The phase information can, identical to this study, be used to derive the location of the resonator while the demodulation amplitude measures the resonance frequency (SPIRE wave) which encodes the residual range.

Another way to encode a distinct resonance frequency while avoiding the need to implant a resonator/ marker, might be the acoustic sensor itself. The sensor could act as a resonance body, as it is typically surrounded by air and coupled only on side with US gel to the patient.

4.3. Applicability and translation

This study assumed idealized conditions given by a homogeneous setup with known acoustic properties and a sensor alignment on the beam axis which consequently reduces Bragg peak localization to a one-dimensional problem. A realistic setting in three dimensions requires N-sensors to be connected to N-lock-in amplifiers each performing an iTPD.

Heterogeneities in the acoustic path with imprecise sound speed knowledge result in a distorted sensor to Bragg peak distance and ultimately to absolute Bragg peak localization errors. A conversion to space domain can be avoided by a co-registration of iTPD to a medical ultrasound image. Complementing IA measurements with ultrasound were first demonstrated by Kellnberger *et al* (2016), Patch *et al* (2016, 2019, 2021) and revealed the relative Bragg peak location in the underlying tissue morphology. Summarized, two IA signals, characterized by their relative bandwidth, are being discussed:

Narrow-band IA signal: It was demonstrated that increasing the modulation frequency in the acoustic signal via pulsing yields to increased lock-in detection capabilities.

A pronounced MHz frequency could be imprinted for the 22 MeV proton beam experiment via pulsing and resonators. As a result, the frequency spectrum of the IA signal was, considered relative, of narrow band-width exhibiting a central frequency in the MHz regime and consequently, the IA signal could be detected by using a single MHz-frequency in the demodulation. For such cases where iTPD can be performed at a strong and distinct frequency, the requirements of the IA sensor change. Instead of sacrificing sensitivity for broadbandness, an IA detection system to be used with iTPD can be of narrow bandwidth, ideally optimized to the desired lock-in/resonance frequency, with increased sensitivity. Therefore, acoustic resonators could be well suited for iTPD as the deposited dose from a single pulse excitation is smaller to that of multiple cycles (modulation via proton burst).

Broad-band IA signal: Considering clinical IA signals, that are based on single proton pulses without resonators, the IA signal constitutes a relatively large bandwidth of approximately 10 kHz to 100 kHz. In such cases for which a single frequency demodulation (35 kHz for 138 MeV and 25 kHz for 220 MeV) might not be optimally suited as only a single part of the entire signal is utilized. Therefore, we argue that an SNR-improving method needs to harvest in such an environment all spectral components. To further increase the sensitivity of iTPD for such broadband IA signals an alternative strategy could be the parallel usage of iTPD, each running at a distinct demodulation frequency (frequency sweep), e.g. at frequencies of the compression and the refraction peak. This concept can be extended to the limiting case of measuring the discrete Fourier transform given by the phase and amplitude of each discrete frequency allowing to derive a spectogram.

5. Conclusion

This study presented a new methodology (iTPD) for online *ToF* measurements of IA waves in frequency domain. iTPD is based on lock-in amplifiers acting as analog-to-digital converters and digital signal processors performing a two-stage signal demodulation called tandem demodulation (TD). If the relation between demodulation frequency and the time point of interest in the IA pressure wave is known (*ToF*), iTPD allows to measure the *ToF* in real time. Accuracy and precision below 15 μm was demonstrated for a pulsed 22 MeV

proton beam for an idealized configuration beyond clinical dose levels. Various aspects of iTPD were systematically investigated in dedicated experiments. A digital iTPD was performed at fractional dose levels on measured and simulated IA signals using clinical proton beam energies herewith motivating further research to increase the sensitivity.

Acknowledgments

Appendix A. Demodulation principle

Demodulation is a two step process of signal mixing and filtering and is illustrated in figure A1. A given input signal s_{sig} entailing a frequency f_{sig}, is in the first step separately multiplied (mixed) with two continuous references signals of the same frequency f_{ref} but different phases (0° and 90°). This process is also known as dual-phase demodulation. The two reference signals can be treated as one single reference signal in the complex plane, whereas the 0° signal denotes the real part and the 90° shifted signal the imaginary part. The real part is further called in-phase component X and the imaginary part, quadrature component Y. Both, X and Y reveal in frequency domain two new frequency components at $f_{sig} - f_{ref}$ and $f_{sig} + f_{ref}$. Given idealized signals and a demodulation frequency f_{ref} at f_{sig}, the output exhibits two distinct frequency components—one at $2f_{sig}$ and a second one at 0 Hz. The latter is equivalent to a signal specific DC offset. After signal multiplication (mixing), the signal information of interest is therefore shifted to 0 Hz which enables the application of a low-pass filter which is described next.

The second step of demodulation is represented by low-pass filtering. The cut-off frequency is chosen below $f_{sig} + f_{ref} \approx 2f_{sig}$ to remove these high frequencies and to be only left with the DC component. The low pass filtered in-phase X and quadrature component Y represent the lock-in amplifiers output and can alternately be converted to polar coordinates to obtain the amplitude $R = \sqrt{X^2 + Y^2}$ and phase $\phi = arctan(\frac{Y}{X})$ of the demodulated signal. The amplitude R is a measure of how strong the demodulation frequency occurs within the IA signal and the phase depicts its delay to an internal reference. The frequency of the reference signal f_{ref} can be understood as prior knowledge incorporated into the demodulation process. For this application, we set f_{ref} to 2.5 MHz as the 2.5 MHz modulated IA signal is to be separated from noise.
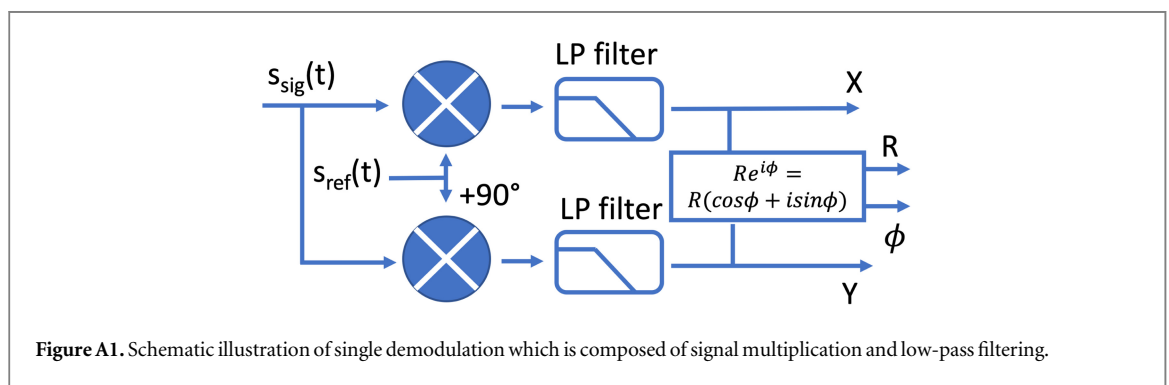

Figure A1. Schematic illustration of single demodulation which is composed of signal multiplication and low-pass filtering.
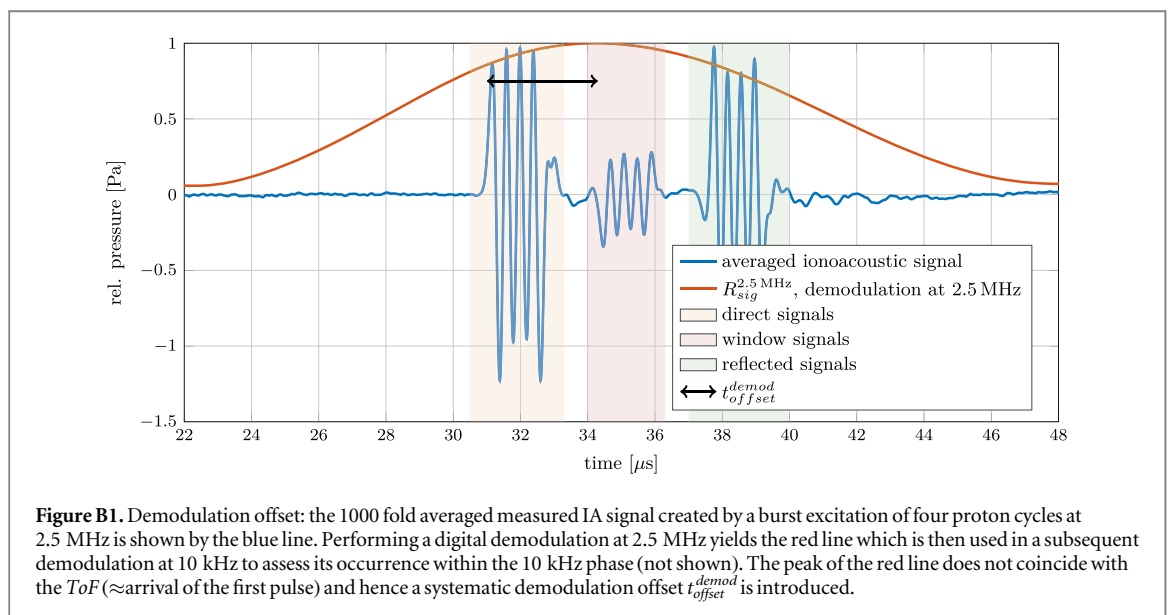
Appendix B. Demodulation offset

Under certain circumstances the accuracy of the iTPD readout may be compromised. If the frequencies of interest occur at various time points, as for instance due to acoustic reflections, the phase readout might be shifted.

As shown in previous single cycle IA related experiments at 20 MeV (Assmann *et al* 2015, Lehrack *et al* 2020), a triplet signature in the IA wave was observed (direct, window and reflection) using a transducer on the beam axis. The result of modulating the IA signal by a proton burst of four-cycles at 2.5 MHz is highlighted in figure B1 by the blue solid line which represents a 1000-fold averaged IA measurement. The direct signals originate from the Bragg peak, the second group of signals stems from the initial pressure discontinuity at the entrance window and the third group of signals are the reflections of the direct signals at the entrance window. Therefore, the IA signal constitutes a 2.5 MHz frequency in the direct, window and reflected signal and consequently at multiple time points. Carrying out a digital demodulation (signal mixing and low-pass filtering) at 2.5 MHz yields the red solid line in figure B1 which depicts the frequency amplitude $R_{sig}^{2.5\ \mathrm{MHz}}$. It appears, the resulting red curve is a surrogate of a 2.5 MHz envelop of the entire signal including window and reflection signals.

Of course, the demodulated signal (red line in figure B1) does not peak at a time corresponding to the *ToF* (arrival of the first pulse) because the window- and reflection-signal introduce a demodulation offset t_{offset}^{demod}. As the entire signal is not symmetric due to acoustic attenuation of the reflection signal, the maximum amplitude of the demodulation does not occur at the center ($\approx 35\ \mu$s) but is slightly shifted towards the direct signals arriving earlier (34.2 μs). Thus, the additional 2.5 MHz frequencies in the window and reflected signal introduce a temporal offset.

Consequently, lock-in measurements performed in this configuration do not directly measure the *ToF* or the arrival of the first signal but the time when the demodulated signal peaks. The introduced offset between *ToF* and the actual phase readout is referred to as demodulation offset t_{offset}^{demod} and is highlighted by the black arrow in B1. In order to derive the *ToF* from the lock-in measurement, it is necessary to subtract the demodulation offset from the iTPD measurement as indicated in equation (3). Quantifying the demodulation offset upfront requires prior knowledge from simulations or a calibration measurement of the relation between the time point of interest, which is in this case the *ToF* and its demodulation peak.

Since the phase difference between the chopper and IA signal was measured, the respective phase measurements were corrected by the systematic demodulation offset in post-processing to obtain the *ToF* through iTPD. However, this may not be as relevant for clinical beam energies with single pulse excitation and larger proton ranges. The manually corrected demodulation offset and its implication on the clinical use case is further discussed in the result section and at the end of this manuscript.

Figure B1. Demodulation offset: the 1000 fold averaged measured IA signal created by a burst excitation of four proton cycles at 2.5 MHz is shown by the blue line. Performing a digital demodulation at 2.5 MHz yields the red line which is then used in a subsequent demodulation at 10 kHz to assess its occurrence within the 10 kHz phase (not shown). The peak of the red line does not coincide with the *ToF* ($\approx$arrival of the first pulse) and hence a systematic demodulation offset t_{offset}^{demod} is introduced.

Appendix C. Cross-correlation

The reference analysis for a proton burst at 2.5 MHz with four cycles and a duty cycle of 50% is illustrated in figure C1. The raw chopper output signal recorded with the PicoScope at the experimental site is shown by the solid red line in figure C1(a). This signal acts as a surrogate of the proton arrival in the water tank. Figure C1(b) presents the average of 1000 measured IA signals in axial sensor position. One thousand measurements using a pulse repetition frequency of 10 kHz yielded a total acquisition time of 100 ms.

In principle, the signals in figures C1(a) and (b) can be directly used for cross-correlation, however, we added an intermediate step to focus on a single frequency (2.5 MHz) similar to the working principle of the lock-in amplifier. Therefore, two idealized four-cycle sinusoidal waves with a period of 0.4 μs were defined in post-processing and shifted according to the position of the maximum cross-correlation with the recorded chopper- and the IA-signal. The result is shown in figures C1(a) and (b) by the red dashed line. In the last step, another cross-correlation is performed between these two idealized sinusoidal waves. The outcome is shown by the green solid line in C1(c). The maximum position of this profile, denoted as ToF_{exp}^{xcorr}, amounts to 31.098 μs. The maximum cross-correlation value indicates the starting position of the template (four-cycle sinusoidal wave) and therefore only approximates the true ToF^{BP} which corresponds to the Bragg peak maximum. To be exact, one needs to precisely know which time point of the bipolar IA signal relates to the Bragg peak maximum.

The small inlet C1(c-1) presents the normalized amplitude spectrum revealing a pronounced frequency content around 2.5 MHz due to the time excitation at 2.5 MHz.

Lastly, figure C1(d) presents the averaged IA signal overlaid by its 2.5 MHz spectrogram illustrating when the frequencies of interest appear. The chopper signal shown in C1(a) and the raw IA signal were fed into the lock-in amplifiers to derive the $\phi_{ref}^{10\,kHz}$ and $\phi_{sig}^{10\,kHz}$ and ultimately ToF_{exp}. The experimentally measured ToF_{exp} derived from the lock-in amplifier was then compared to $ToF_{exp}^{xcorr} = 31.098$ μs.
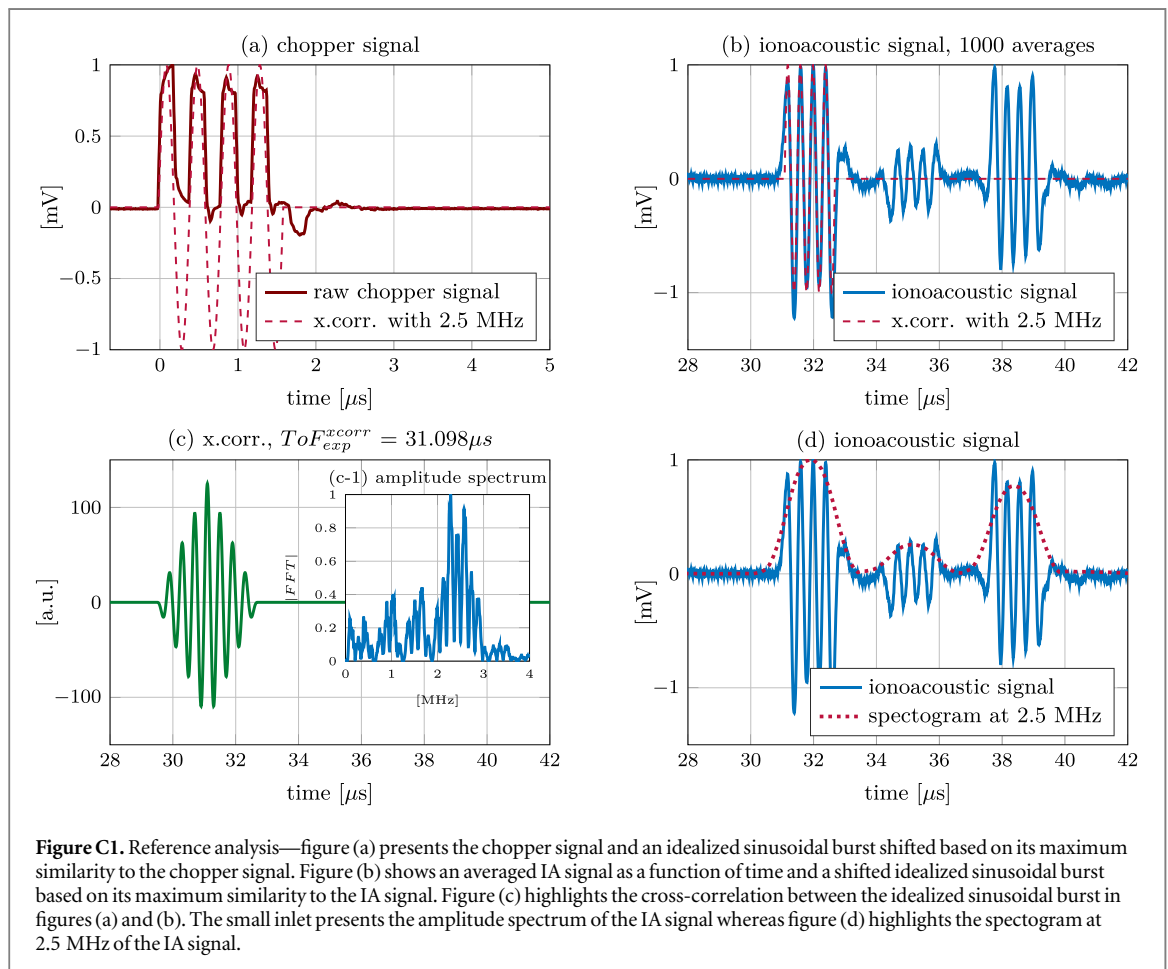
Figure C1. Reference analysis—figure (a) presents the chopper signal and an idealized sinusoidal burst shifted based on its maximum similarity to the chopper signal. Figure (b) shows an averaged IA signal as a function of time and a shifted idealized sinusoidal burst based on its maximum similarity to the IA signal. Figure (c) highlights the cross-correlation between the idealized sinusoidal burst in figures (a) and (b). The small inlet presents the amplitude spectrum of the IA signal whereas figure (d) highlights the spectrogram at 2.5 MHz of the IA signal.

Appendix D. Simulation framework

A FLUKA Monte Carlo (version 2020.03) simulation (Ferrari *et al* 2005, Böhlen *et al* 2014) was performed for 22 MeV protons mimicking the experimental setup at the Tandem Van de Graff accelerator. Lateral beam information is acquired from Gafchromic film measurements during the experiment. The simulated dose deposition given in [Gy] was converted to an initial pressure distribution in [Pa] over the following relationship neglecting in first approximation any heat defects:

$$p_0(\boldsymbol{r}, T) = D(\boldsymbol{r})\Gamma(\boldsymbol{r}, T)\rho(\boldsymbol{r}, T), \tag{D.1}$$

where T denotes the temperature in [°C], Γ the material-specific dimensionless Grüneisenparameter, ρ the material density [kg m^{-3}] and D the dose distribution in [Gy]. The initial pressure distribution p_0 was then used as input for the pseudospectral wave propagation simulation employing the k-Wave toolbox (Treeby and Cox 2010, Treeby *et al* 2016). For wave propagation, a spatial grid spacing of 15 μm and time spacing of 2.5 ns were chosen to support all frequencies present in p_0. Acoustic properties and the Grüneisenparamter of water were selected according to the temperature recorded during the experiment. The simulation was carried out assuming a δ-time excitation to obtain the IA pressure $p_{sim}^{\delta}(\boldsymbol{r_s}, t)$ as a function of time t and a given sensor location $\boldsymbol{r_s}$. Following the work of (Jones *et al* 2016a), this allowed in a separate step to convolve the measured proton time profiles $E(t)$ with $p_{sim}^{\delta}(\boldsymbol{r_s}, t)$ to obtain realistic non-δ time excitations $p_{sim}(\boldsymbol{r_s}, t)$. The transducer's total impulse response (*TIR*) was approximated by a butterworth band pass filter of first order (Ahmad *et al* 2015). The central frequency was set to 3.5 MHz to be in line with the experimental PZT transducer. The processing pipeline to derive the simulated IA signal p_{sim}^{TIR} is then given by:

$$p_{sim}^{TIR} = p_{sim}^{\delta}(\boldsymbol{r_s}, t) \circledast E(t) \circledast TIR(\boldsymbol{r}, t). \tag{D.2}$$
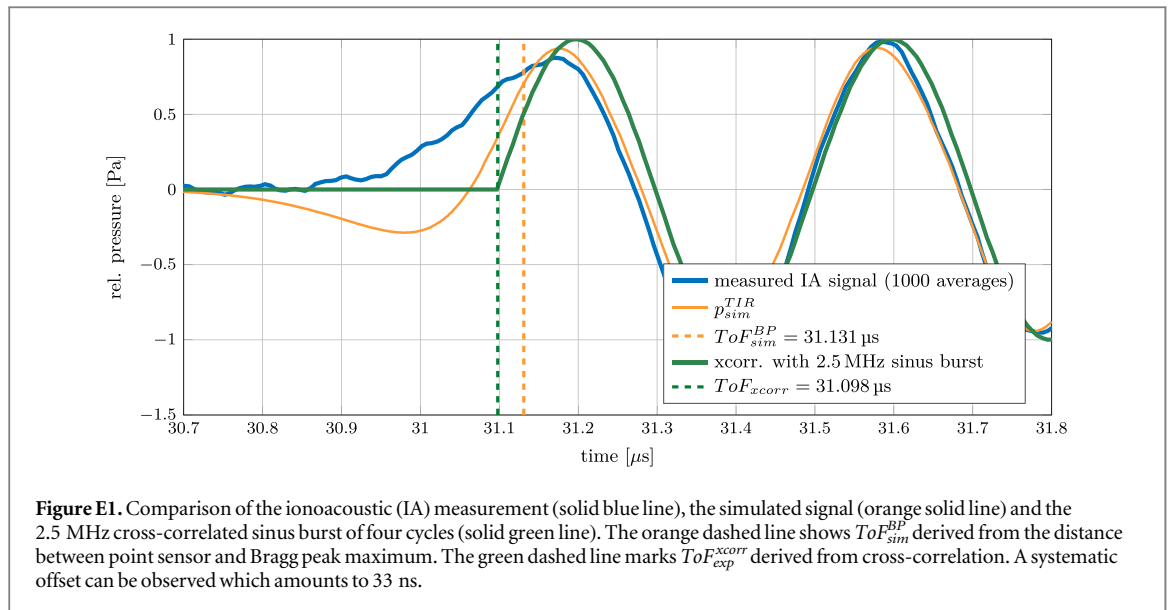
As the exact distance between sensor and Bragg peak maximum providing ToF^{BP} is unknown in the experiment, the simulation was performed for multiple point sensor locations arranged on an axial line with increasing distances. Next, a single point sensor was determined whose simulated pressure trace resulted in the maximum cross-correlation (best match) with the measurement. From the identified point sensor, the geometrical distance to Bragg peak maximum was calculated purely from the simulation grid (15 μm grid spacing). The distance between sensor and maximum Bragg peak position was converted to time in order to derive the simulated reference ToF_{sim}^{BP}.

Accurately identifying the time point from the pressure curve that represents the distance between sensor and Bragg peak maximum can be done *in-silico* with known positions and geometries. As pointed out by Jones *et al* (2016a) conventional features of the acoustic signal such as the maximum or the zero-crossing do generally not represent the correct distance between sensor and maximum of the Bragg peak. This phenomena is also confirmed in the simulation.

ToF_{sim}^{BP} deviates from the cross-correlation analysis using experimental signals by 33 ns. This discrepancy arises since ToF_{sim}^{BP} and ToF_{exp}^{xcorr} refer to different time points. An explanation is given in the appendix E. Although we consider ToF_{sim}^{BP} as the ground truth, we also present ToF_{exp}^{xcorr} in the result section, as it resembles more closely the functionality of an iTPD, which is in the first place finding 2.5 MHz frequencies. The constant systematic difference of 33 ns between ToF_{sim}^{BP} and ToF_{exp}^{xcorr} is acknowledged and elaborated in results and discussion.

Appendix E. Quantifying the time of flight

Figure E1 presents a comparison of different methods approximating the true ToF ToF^{BP} which provides the exact distance to the Bragg peak maximum. The blue solid line highlights the 1000 fold averaged IA signal from figure 4. The orange line shows the simulated pressure trace for a point sensor whose signal matched best with the measurement. The corresponding Bragg peak maximum to sensor distance is highlighted by the vertical dashed orange line. Correlating a sinus burst (green line) with the measurement results in a maximum similarity given by the vertical green dashed line, which marks the start position of the template being used for cross-correlation. It can be seen that different methods yield different *ToF* estimates. A systematic error also occurs when selecting the maximum of the first peak or the zero crossing of the measured IA signal. The problem of exactly selecting the time point from the pressure curve that relates to the maximum Bragg peak position is also described in Jones *et al* (2016a).

Figure E1. Comparison of the ionoacoustic (IA) measurement (solid blue line), the simulated signal (orange solid line) and the 2.5 MHz cross-correlated sinus burst of four cycles (solid green line). The orange dashed line shows ToF_{sim}^{BP} derived from the distance between point sensor and Bragg peak maximum. The green dashed line marks ToF_{exp}^{xcorr} derived from cross-correlation. A systematic offset can be observed which amounts to 33 ns.

Appendix F. Overview of iTPD

Figure F1 presents an overview of the iTPD readout introduced in equation (2) without performing the accurate iTPD. A long measurement period was selected to investigate the accuracy and stability of iTPD. The solid red line in figure F1 depicts the reference phase readout $\phi_{ref}^{10\,\text{kHz}}$ in radians (-2π to 0) which is constant over the complete measurement period as the chopper was always switched on and hence a reference phase was measured.

The reference phase $\phi_{ref}^{10\,\text{kHz}}$ amounts to -2.612 rad and represents the 10 kHz phase of the chopper signal with respect to the lock-in amplifier internal reference. In addition, the black solid line depicts the IA signal phase $\phi_{sig}^{10\,\text{kHz}}$, which fluctuates more than the reference phase due to the lower IA signal amplitude. There are two spikes in the phase readout of $\phi_{sig}^{10\,\text{kHz}}$ at 0.3 and 7.2 s visible which can be related to beam instabilities. The phase difference between the signal phase and reference phase is highlighted by the blue solid line in figure F1 taking into account the demodulation offset introduced in appendix B. It is important to stress, that $\phi_{sig}^{10\,\text{kHz}}$ and $\phi_{ref}^{10\,\text{kHz}}$ can take any value between 0 and 2π for repetitive measurements, however, their relative difference $\Delta\phi^{10\,kHz}$ remains unchanged. Performing a phase calibration measurement upfront allows to only use a single lock-in amplifier.

Figure F1. Overview of ionoacoustic tandem phase detection (iTPD) at 2.5 MHz and 10 kHz. ϕ_{ref}^{10kHz} and ϕ_{sig}^{10kHz} present the reference and IA phase readout, respectively. Their difference $\Delta\phi^{10\,kHz}$ is given by the thick blue line. The red dashed line indicates the time based reference analysis using signal averaging and cross-correlation.
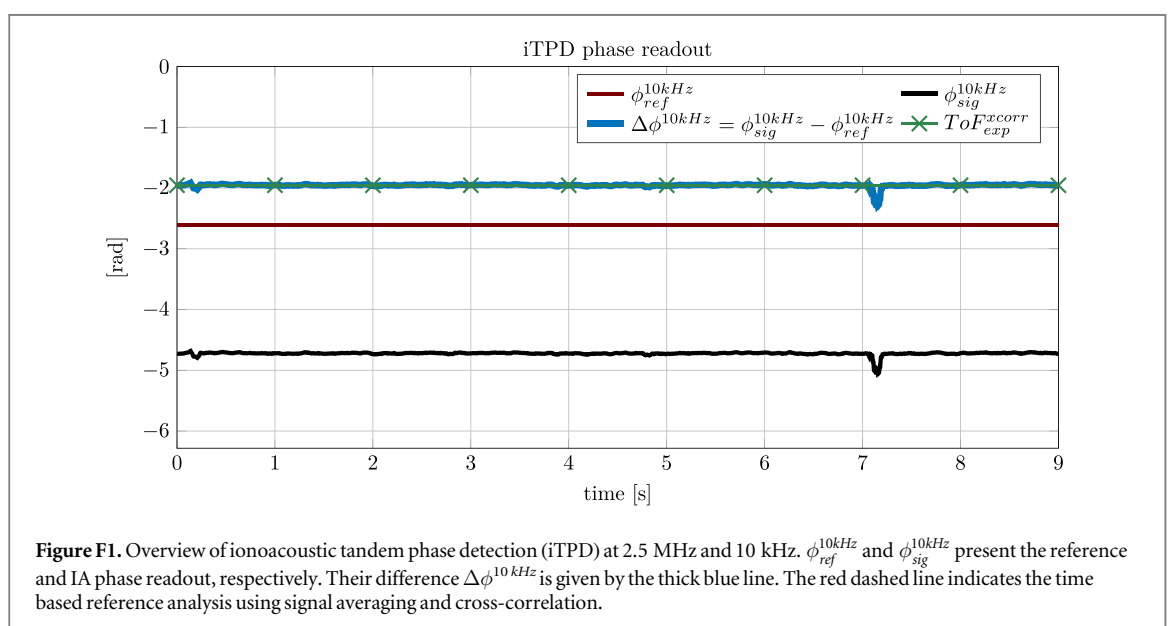
The green crosses mark the phase in radians derived from ToF_{exp}^{xcorr}, which amounts to 31.098 μs and corresponds in a 10 kHz period to -1.954 rad. It aligns with the phase difference measured online with the lock-in amplifier via iTPD (blue solid line).

Appendix G. Error estimation of the ToF

Error sources contributing to inaccuracies in ToF_{exp}^{xcorr} are discussed below. The sampling time of the PicoScope was 6.4 ns which directly translates into a trigger uncertainty. We assume an error on the *ToF* from the sampling time to be $\sigma_{samp} = 6.4$ ns.

Another statistically independent error source are minor variations of the terminal voltage of the electrostatic Tandem accelerator which were conservatively estimated to be in the range of 2–20 keV. This yields to a shifted Bragg peak location of 10 μm and henceforth to an accelerator induced uncertainty in the *ToF* of about $\sigma_{accel} = 6.5$ ns. This can be understood as jitter of the IA signal.

Third, inaccuracies in the water temperature measurements yield to sound speed errors. We estimate the error to be in the order of 0.1 $^\circ$ Celsius which results in a speed of sound error of $\sigma_c^{water} = 0.18$ μm μs^{-1} and in further consequence to an error in time of $\sigma_c^{water} = 3.6$ ns considering a *ToF* of 30 μs.

Considering statistical independence of each error source, we estimate the overall uncertainty of ToF_{exp}^{xcorr} to be 9.8 ns.

Uncertainty sources contributing to ToF_{sim}^{BP} are due to errors in the Monte Carlo dose calculation as for instance (i) the mean ionization potential (ii) uncertainties in modeling the experimental setup and (iii) density variations due to temperature inaccuracies. We estimate the overall Bragg peak localization uncertainty to be in the order of 15 μm. Moreover, the error arising from the wave propagation simulation is dominated by sound speed errors. Identical to before, we estimate this error to be $\sigma_c^{water} = 3.6$ ns. Furthermore, we estimate the error of modeling the transducer by an omnidirectional point sensor convolved with a synthetic impulse response to be in the order of 15 ns. Thus the total estimated error in ToF_{sim}^{BP} amounts to about 18 ns.
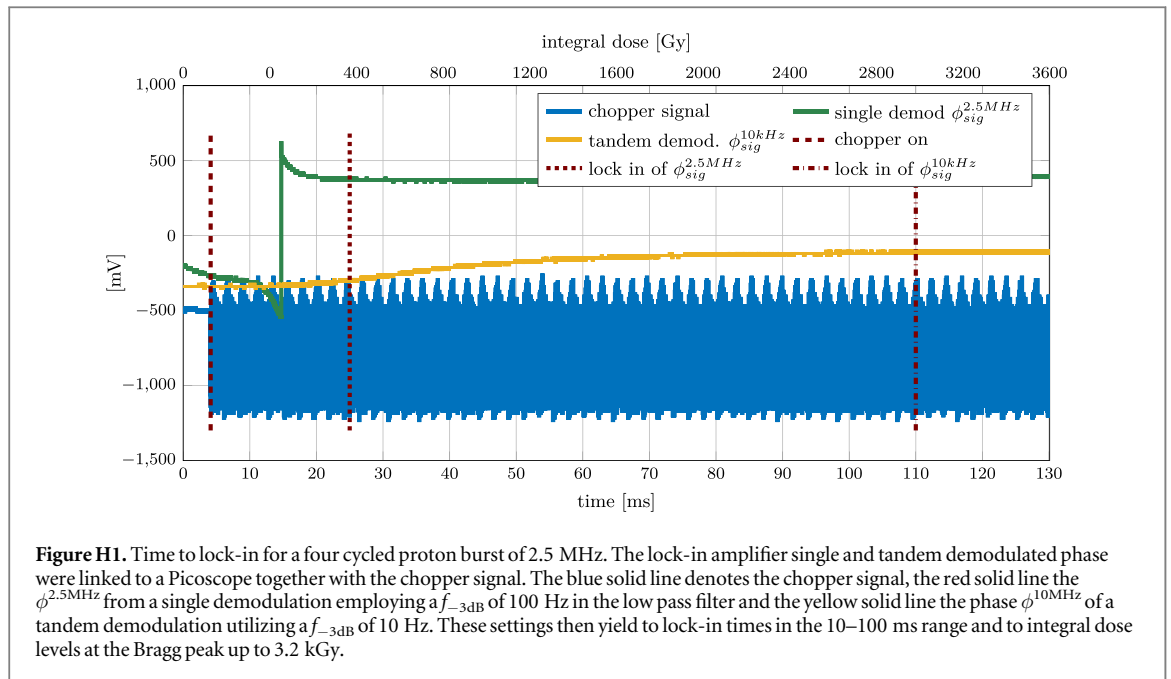
Appendix H. Time to lock-in

The first demodulation considers a 3rd order low-pass filter utilizing a cut-off frequency of 12 kHz at -3 dB and the second demodulation employs 100 Hz at -3 dB. Therefore, the low-pass filter of the second demodulation entailed longer settling times which directly translated to an increased accumulated dose over time. Table H1 presents an overview of theoretical settling times alongside the respective accumulated dose for different filter configurations. The bold table row indicates the settings utilized for the experimental measurement reported in section 3.1.1. The accumulated peak dose over time is based on the maximum Bragg peak dose of 0.8 Gy per cycle per pulse. Setting f_{-3dB} to 100 Hz ($T = 10$ ms) and considering a bandwidth of $f_{-3dB} = 0.081\tau^{-1}$ which is provided by the manufacturer (Zurich Instruments 2016), yields to a time constant of $\tau = 0.81$ ms.

From Zurich Instruments (2016) it is known that it takes 3.26τ to settle to the 63.2% level which corresponds in this configuration to 2.64 ms. Considering the 10 kHz burst repetition frequency, an integral dose d63 for the 63.2% level amounts to 21.1 Gy per cycle. Since four proton cycles were considered the total integral dose sums to 84.4 Gy. Increasing the filter order using the same cut-off frequency (e.g. 100 Hz) results in steeper frequency responses for the price of longer settling times, which is highlighted in the last row of table H1.

The remaining filter configurations were derived analogously taking into account the 0.8 Gy maximum dose level per cycle per 100 μs. From table H1 it is apparent that the integral dose values substantially exceed the typically prescribed fractionated dose levels of a few Gy. In addition to the settling time shown in table H1, the phase delay introduced by the low-pass filter itself also needs to be considered. Steeper frequency cut-offs are

Table H1. Overview of filter characteristics and their corresponding settling times and accumulated doses. The row marked in bold represents the filter settings employed for the result shown in the previous section. Values presented in the third column f_{-3dB} in $[\tau^{-1}]$ were taken from Zurich Instruments (2016). The accumulated dose levels refer to [Gy] per proton cycle.

Filter characteristics				Calculated settling times				Accumulated dose			
Order [#]	f_{-3dB} [Hz]	f_{-3dB} [τ^{-1}]	τ [ms]	63.2%	90%	99% [ms]	99.9%	d63	d90	d99 [Gy]/cycle	d99.9
1	100	0.159	1.59	1.59	3.65	7.33	10.98	12.72	29.2	58.64	87.84
3	**100**	**0.081**	**0.81**	**2.64**	**4.31**	**6.81**	**9.10**	**21.1**	**34.5**	**54.5**	**72.8**
3	300	0.081	0.27	0.88	1.43	2.27	3.03	7.0	11.5	18.2	24.3
5	100	0.061	0.61	3.31	4.87	7.07	9.02	26.5	39.0	56.6	72.2

Figure H1. Time to lock-in for a four cycled proton burst of 2.5 MHz. The lock-in amplifier single and tandem demodulated phase were linked to a Picoscope together with the chopper signal. The blue solid line denotes the chopper signal, the red solid line the $\phi^{2.5\text{MHz}}$ from a single demodulation employing a $f_{-3\text{dB}}$ of 100 Hz in the low pass filter and the yellow solid line the phase $\phi^{10\text{MHz}}$ of a tandem demodulation utilizing a $f_{-3\text{dB}}$ of 10 Hz. These settings then yield to lock-in times in the 10–100 ms range and to integral dose levels at the Bragg peak up to 3.2 kGy.

achieved by higher filter orders in exchange for increased settling times and phase delays. A 3rd order low pass filter at 100 Hz yields to a phase delay of $\approx -\pi/2$ which results to 2.5 ms and is therefore subordinate to the settling times from table H1.

The iTPD readouts indicate a strong influence of the selected filter parameters on the required measurement time and with that on the total accumulated dose. Note that 100 ms corresponds to 1000 individual proton bursts at 10 kHz for which the results were shown previously in figure C1. In contrast, the required lock-in time amounts according to table H1 to 9.1 ms.

The time to lock-in was experimentally verified in a separate experiment for which the auxiliary outputs of the lock-In amplifier, responsible for the tandem demodulation (TD) of the IA signal, were connected to the PicoScope to measure the phase as voltage. In detail, the analog output of the first (2.5 MHz) and second (10 kHz) demodulation and the chopper signal were recorded with a sampling time 0.7 μs. The result for an individual measurement over 130 ms is shown in figure H1. The blue solid line depicts the chopper signal. The fine micro structure, rectangular bursts at 2.5 MHz cannot be resolved in this ms time scale. For the first 4 ms the chopper was blocking the protons before the acceleration tank. This can be understood as a turned-off beam. The first vertical red dashed line marks the time point of switching on the chopper/beam and applying a four cycled rectangular proton burst at 2.5 MHz every 10 kHz.

The green solid line represents the result of a single demodulation performed at 2.5 MHz using a 3rd order low-pass filter at 100 Hz. According to table H1 this yields a settling time of 9.1 ms. However, in the given experimental setup, turning on the chopper at 4 ms does not indicate a direct arrival of protons in the water tank. We observed for some measurements a time offset of up to 200 ms between turning on the chopper and the actual arrival of protons in the water tank. Such delays might be caused by electromagnetic stabilizing processes in the beam line. For the experiment shown in figure H1, we assume an arrival of protons at the experimental site at 15 ms because of the following reasons:

Given (i) the stabilization processes in the beam line, (ii) the theoretical settling time to be in the order of 10 ms and (iii) the progression of the $\Delta\phi^{2.5\text{MHz}}$ (green solid line) in figure H1 from 15 ms onward, an arrival of protons in the water tank around 15 ms is highly likely. The red dotted line at 25 ms marks the time at which the lock-in is settled. Consequently, the settling duration for the lock-in to obtain $\Delta\phi^{2.5\text{MHz}}$ is about 10 ms assuming a proton arrival at 15 ms. Moreover, the yellow solid line represents $\Delta\phi^{10\text{kHz}}$ from an iTPD employing a 10 Hz low-pass filter for which a theoretical settling time of 90 ms is expected. The vertical red dash-dotted line marks the settling time of $\Delta\phi^{10\text{kHz}}$ which amounts to 110 ms $-$ 15 ms = 95 ms.

The corresponding integral dose is shown on the upper x-axis of figure H1. It can be seen that the clinical fractionated dose level of a few Gy are exceeded by two orders of magnitude yielding to an accumulated dose at the Bragg peak of 3.2 kGy. The results presented in section 3.1.1 are based on a low pass filter of 100 Hz which corresponds for the four cycle proton burst to an accumulated Bragg peak dose of 291 Gy. This aspect is further elaborated in the discussion.

Lastly, the time offset between the chopper signal and the arrival of protons of 1.43 μs (see section 2.1.2) plays a negligible role for the time to lock-in measurements that take place in the ms domain.

ORCID iDs

H P Wieser ⓘ https://orcid.org/0000-0002-2309-7963
Y Huang ⓘ https://orcid.org/0000-0002-4774-7449
J Lascaud ⓘ https://orcid.org/0000-0002-7649-6909
M Würl ⓘ https://orcid.org/0000-0003-3044-449X
K Parodi ⓘ https://orcid.org/0000-0001-7779-6690

References

Ahmad M, Xiang L, Yousefi S and Xing L 2015 Theoretical detection threshold of the proton-acoustic range verification technique *Med. Phys.* **42** 5735–44

Assmann W *et al* 2015 Ionoacoustic characterization of the proton Bragg peak with submillimeter accuracy *Med. Phys.* **42** 567–74

Baumann M, Krause M, Overgaard J, Debus J, Bentzen S M, Daartz J, Richter C, Zips D and Bortfeld T 2016 Radiation oncology in the era of precision medicine *Nat. Rev. Cancer* **16** 234–49

Bisogni M G *et al* 2016 INSIDE in-beam positron emission tomography system for particle range monitoring in hadrontherapy *J. Med. Imaging* **4** (1) 011005

Böhlen T T, Cerutti F, Chin M P W, Fassò A, Ferrari A, Ortega P G, Mairani A, Sala P R, Smirnov G and Vlachoudis V 2014 The FLUKA Code: developments and challenges for high energy and medical applications *Nucl. Data Sheets* **120** 211–4

Brown K H, Ghita M, Schettino G, Prise K M and Butterworth K T 2020 Evaluation of a novel liquid fiducial marker, BioXmark®, for small animal image-guided radiotherapy applications *Cancers* **12** (5) 1276

Buitenhuis H J T, Diblen F, Brzezinski K W, Brandenburg S and Dendooven P 2017 Beam-on imaging of short-lived positron emitters during proton therapy *Phys. Med. Biol.* **62** 4654–72

Dal Bello R, Martins P M, Brons S, Hermann G, Kihm T, Seimetz M and Seco J 2020 Prompt gamma spectroscopy for absolute range verification of 12 C ions at synchrotron-based facilities *Phys. Med. Biol.* **65** (9) 095010

Dollinger G, Parodi K, Assmann W, Ntziachristos V and Kellnberger S 2016 A method and apparatus for determining an energy deposition of an ion beam EP2974771A1 (https://patents.google.com/patent/EP2974771A1/en)

Ferrari A, Sala P R, Fasso A and Ranft J 2005 FLUKA: a multi-particle transport code *Technical Report CERN 2005-10 (2005), INFN/TC 05/11, SLAC-R-773* Stanford Linear Accelerator Center (SLAC), Menlo Park, CA (https://citeseerx.ist.psu.edu/viewdoc/summary?doi=10.1.1.393.4720)

Ferrero V *et al* 2018 Online proton therapy monitoring: clinical test of a Silicon-photodetector-based in-beam PET *Sci. Rep.* **8** 4100

Freijo C, Herraiz J L, Sanchez-Parcerisa D and Udias J M 2021 Dictionary-based protoacoustic dose map imaging for proton range verification *Photoacoustics* **21** 100240

Hayakawa Y, Tada J, Arai N, Hosono K, Sato M, Wagai T, Tsuji H and Tsujii H 1995 Acoustic pulse generated in a patient during treatment by pulsed proton radiation beam *Radiat. Oncol. Investigations* **3** 42–5

Hickling S, Xiang L, Jones K C, Parodi K, Assmann W, Avery S, Hobson M and El Naqa I 2018 Ionizing radiation-induced acoustics for radiotherapy and diagnostic radiology applications *Med. Phys.* **45** e707–21

Hueso-González F, Rabe M, Ruggieri T A, Bortfeld T and Verburg J M 2018 A full-scale clinical prototype for proton range verification using prompt gamma-ray spectroscopy *Phys. Med. Biol.* **63** (18) 195019

Johnson R P 2018 Review of medical radiography and tomography with proton beams *Rep. Prog. Phys.* **81** 016701

Jones K C, Nie W, Chu J C H, Turian J V, Kassaee A, Sehgal C M and Avery S 2018 Acoustic-based proton range verification in heterogeneous tissue: simulation studies *Phys. Med. Biol.* **63** 025018

Jones K C, Seghal C M and Avery S 2016a How proton pulse characteristics influence protoacoustic determination of proton-beam range: simulation studies *Phys. Med. Biol.* **61** 2213–42

Jones K C, Vander Stappen F, Sehgal C M and Avery S 2016b Acoustic time-of-flight for proton range verification in water *Med. Phys.* **43** 5213–24

Kellnberger S, Assmann W, Lehrack S, Reinhardt S, Thirolf P, Queirós D, Sergiadis G, Dollinger G, Parodi K and Ntziachristos V 2016 Ionoacoustic tomography of the proton Bragg peak in combination with ultrasound and optoacoustic imaging *Sci. Rep.* **6** (1) 29305

Klein J, Tran W, Lai P, Al-Mahrouki A, Giles A and Czarnota G J 2020 Effect of Treatment Sequencing on the Tumor Response to Combined Treatment With <scp>Ultrasound-Stimulated</scp> Microbubbles and Radiotherapy *J. Ultrasound Med.* **39** 2415–25

Kozłowska W S, Böhlen T T, Cuccagna C, Ferrari A, Fracchiolla F, Georg D, Magro G, Mairani A, Schwarz M and Vlachoudis V 2019 FLUKA particle therapy tool for Monte Carlo independent calculation of scanned proton and carbon ion beam therapy *Phys. Med. Biol.* **64** 075012

Krimmer J, Dauvergne D, Létang J M and Testa 2018 Prompt-gamma monitoring in hadrontherapy: A review *Nucl. Instrum. Methods Phys. Res.* A **878** 58–73

Lascaud J *et al* 2021 Enhancement of the ionoacoustic effect through ultrasound and photoacoustic contrast agents *Sci. Rep.* **11** 2725

Lehrack S, Assmann W, Bender M, Severin D, Trautmann C, Schreiber J and Parodi K 2020 Ionoacoustic detection of swift heavy ions *Nucl. Instrum. Methods Phys. Res.* A **950** 162935

Lehrack S *et al* 2017 Submillimeter ionoacoustic range determination for protons in water at a clinical synchrocyclotron *Phys. Med. Biol.* **62** L20–30

Lomax A J 2008a Intensity modulated proton therapy and its sensitivity to treatment uncertainties: I. The potential effects of calculational uncertainties *Phys. Med. Biol.* **53** 1027–42

Lomax A J 2008b Intensity modulated proton therapy and its sensitivity to treatment uncertainties: II. The potential effects of inter-fraction and inter-field motions *Phys. Med. Biol.* **53** 1043–56

Mascarenhas S, Vargas H and Cesar C L 1984 A photoacoustical radiation dosimeter *Med. Phys.* **11** 73–4

MATLAB 2017 version 9.3.0.713579 (R2017b)

McNabb E, Al-Mahrouki A, Law N, McKay S, Tarapacki C, Hussein F and Czarnota G J 2020 Ultrasound-stimulated microbubble radiation enhancement of tumors: Single-dose and fractionated treatment evaluation *PLoS One* **15** (9) e0239456

Newhauser W D and Zhang R 2015 The physics of proton therapy *Phys. Med. Biol.* **60** R155–209

Otero J, Felis I, Herrero A, Merchán J A and Ardid M 2020 Bragg peak localization with piezoelectric sensors for proton therapy treatment *Sensors* **20** (10) 2987

Paganetti H 2012 Range uncertainties in proton therapy and the role of Monte Carlo simulations *Phys. Med. Biol.* **57** R99–117

Parodi K 2020 Latest developments in *in-vivo* imaging for proton therapy *Br. J. Radiol.* **93** 20190789

Parodi K and Polf J C 2018 *In-vivo* range verification in particle therapy *Med. Phys.* **45** e1036–50

Parodi K *et al* 2007 Patient study of in vivo verification of beam delivery and range, using positron emission tomography and computed tomography imaging after proton therapy *Int. J. Radiat. Oncol.* *Biol.* *Phys.* **68** 920–34

Patch S K, Hoff D E M, Webb T B, Sobotka L G and Zhao T 2018 Two-stage ionoacoustic range verification leveraging Monte Carlo and acoustic simulations to stably account for tissue inhomogeneity and accelerator-specific time structure—a simulation study *Med. Phys.* **45** 783–93

Patch S K, Santiago-Gonzalez D and Mustapha B 2019 Thermoacoustic range verification in the presence of acoustic heterogeneity and soundspeed errors—robustness relative to ultrasound image of underlying anatomy *Med. Phys.* **46** 318–27

Patch S K *et al* 2016 Thermoacoustic range verification using a clinical ultrasound array provides perfectly co-registered overlay of the Bragg peak onto an ultrasound image *Phys. Med. Biol.* **61** 5621–38

Patch S K *et al* 2021 Thermoacoustic range verification during pencil beam delivery of a clinical plan to an abdominal imaging phantom *Radiother. Oncol.* **159** 224–30

Pausch G, Berthold J, Enghardt W, Römer K, Straessner A, Wagner A, Werner T and Kögler T 2020 Detection systems for range monitoring in proton therapy: Needs and challenges *Nucl. Instrum. Methods Phys. Res.* A **954** 161227

Richter C *et al* 2016 First clinical application of a prompt gamma based in vivo proton range verification system *Radiother. Oncol.* **118** 232–7

Riva M, Vallicelli E A, Baschirotto A and De Matteis M 2018 Acoustic analog front end for proton range detection in hadron therapy *IEEE Trans. Biomed. Circuits Syst.* **12** 954–62

Rohrer L, Jakob H, Rudolph K and Skorka S J 1984 The four gap double drift buncher at Munich *Nucl. Instrum. Methods Phys. Res.* **220** 161–4

Rydhög J S *et al* 2017 Liquid fiducial marker applicability in proton therapy of locally advanced lung cancer *Radiother. Oncol.* **122** 393–9

Sohn J, Nie W, Avery S M, He X, Zhou J, Yang X and Liu T 2020 Wavelet-based protoacoustic signal denoising for proton range verification *Medical Imaging 2020: Ultrasonic Imaging and Tomography* vol 1 131 904 ed N V Ruiter and B C Byram (SPIE) p 3

Takayanagi T, Uesaka T, Kitaoka M, Unlu M B, Umegaki K, Shirato H, Xing L and Matsuura T 2019 A novel range-verification method using ionoacoustic wave generated from spherical gold markers for particle-beam therapy: a simulation study *Sci. Rep.* **9** (1) 4011

Takayanagi T *et al* 2020 On-line range verification for proton beam therapy using spherical ionoacoustic waves with resonant frequency *Sci. Rep.* **10** (1) 20385

Tran L T *et al* 2015a 3D Silicon Microdosimetry and RBE Study Using $\{12\}\{\rm C\}$ Ion of Different Energies *IEEE Trans. Nucl. Sci.* **62** 3027–33

Tran L T *et al* 2015b 3D-mesa 'bridge' silicon microdosimeter: Charge collection study and application to rbe studies in 12rm c radiation therapy *IEEE Trans. Nucl. Sci.* **62** 504–11

Treeby B, Cox B and Jaros J 2016 k-Wave, Manual Version 1.1.1

Treeby B E and Cox B T 2010 k-Wave: MATLAB toolbox for the simulation and reconstruction of photoacoustic wave fields *J. Biomed. Opt.* **15** 021314

Unkelbach J *et al* 2018 Robust radiotherapy planning *Phys. Med. Biol.* **63** 22TR02

Vallicelli E A, Baschirotto A, Lehrack S, Assmann W, Parodi K, Viola S, Riccobene G and De Matteis M 2021 22 dB signal-to-noise ratio real-time proton sound detector for experimental beam range verification *IEEE Trans. Circuits Syst. I: Regular Pap.* **68** 3–13

van Dongen K W A, de Blécourt A J, Lens E, Schaart D R and Vos F M 2019 Reconstructing 3D proton dose distribution using ionoacoustics *Phys. Med. Biol.* **64** 225005

Van Herk M 2004 Errors and margins in radiotherapy *Semin. Radiat. Oncol.* **14** 52–64

Verburg J M and Seco J 2014 Proton range verification through prompt gamma-ray spectroscopy *Phys. Med. Biol.* **59** 7089–106

Vynckier S, Derreumaux S, Richard F, Bol A, Michel C and Wambersie A 1993 Is it possible to verify directly a proton-treatment plan using positron emission tomography? *Radiother. Oncol.* **26** 275–7

Wang L V and Wu H-i 2012 *Biomedical Optics: Principles and Imaging* (New York: Wiley)

Wieser H-P *et al* 2017 Development of the open-source dose calculation and optimization toolkit matRad *Med. Phys.* **44** 2556–68

Wohlfahrt P, Möhler C, Richter C and Greilich S 2018 Evaluation of stopping-power prediction by dual- and single-energy computed tomography in an anthropomorphic ground-truth phantom *Int. J. Radiat. Oncol. Biol. Phys.* **100** 244–53

Würl M *et al* 2018 Time-of-flight spectrometry of ultra-short, polyenergetic proton bunches *Rev. Sci. Instrum.* **89** 123302

Yu Y, Li Z, Zhang D, Xing L and Peng H 2019 Simulation studies of time reversal-based protoacoustic reconstruction for range and dose verification in proton therapy *Med. Phys.* **46** 3649–62

Zurich Instruments 2016 Principles of lock-in detection and the state of the art. Technical report, Zurich Instruments